Volume 43 Number 9 September 1987

# PHILIPS TECHNICAL REVIEW

Automatic speech segmentation

Black coating for solar collectors

Television glass

Image-storage system

PHILIPS

Philips Technical Review (ISSN 0031-7926) is published by Philips Research Laboratories, Eindhoven, the Netherlands, and deals with the investigations, processes and products of the laboratories and other establishments that form part of or are associated with the Philips group of companies. In the articles the associated technical problems are treated along with their physical or chemical background. The Review covers a wide range of subjects, each article being intended not only for the specialist in the subject but also for the non-specialist reader with a general technical or scientific training.

The Review appears in English and Dutch editions; both are identical in contents. There are twelve numbers per volume, each of about 32 pages. An index is included with each volume and indexes covering ten volumes are published (the latest one was included in Volume 40, 1982).

PHILIPS TECHNICAL REVIEW

Volume 43, No. 9, September 1987

# Contents



PHILIPS

PHILIPS TECHNICAL REVIEW

Volume 43, No. 9, September 1987

# Automatic segmentation of speech into diphones

J. P. van Hemert

*With the advance of automation the number of people who transact business directly with the public is steadily declining. It is becoming increasingly common, for example, to draw money from automatic cash dispensers. In such situations the customer has to carry out instructions given by the machine. Usually the instructions appear on a screen, but sometimes they are spoken. In such a case the number of instructions that can be given is limited. A method of producing spoken instructions just as freely and flexibly as text on a screen consists in joining small speech segments together and making them audible. This article describes the preparation of the 'library' of segments (diphones).*

## Introduction

Speech has been with us since time immemorial. And today, even in situations where it is possible to communicate in some other direct way, e.g. with a keyboard and display screen, many people will still prefer the spoken word. One possible reason for this is that people can then make other 'observations' — visual ones, perhaps — while they talk or listen. On the other hand, communication between man and machine usually requires a keyboard and a display. At the Institute for Perception Research ways and means are being studied of bringing one direction of this two-way communication, the output from machine to man, into the form of speech. Speaking machines will have many useful applications in the future. Much time can be saved, for example, by using a spoken set of instructions instead of a printed one when setting up complex equipment. In situations, too, where eyes and hands are already occupied and actions have to be performed on the basis of new information, that information can best be presented in the form of spoken messages (as for instance in the CARIN system [1]).

*Ir J. P. van Hemert is with the Institute for Perception Research, Eindhoven.*

Many systems with speech output depend on the use of complete messages spoken-in beforehand. The system would be more flexible and offer wider prospects if the spoken messages could be built up from smaller units, in the same way as written language. The units constitute the basic elements of what might be called a 'speech alphabet', by analogy with the alphabet of written language. A system with such a collection of basic elements would bring an unlimited vocabulary within reach.

Before going into our choice of the basic elements for the speech alphabet, we shall first take a look at natural speech and indicate possible divisions of the speech signal. Speech is a succession of audible air-

[1] CARIN is an automobile navigation and information system comprising a Compact Disc player, a position-determining system and a computer. It uses geographical information stored in digital form on a Compact Disc to the CD-I (Compact Disc Interactive) standard. The system takes this geographical information and the destination entered by the driver, and maps out a route. It then uses the position-determining system to guide the driver to his destination. The directions are given as spoken instructions (at present they are complete sentences spoken-in beforehand, but they will probably be derived from synthetic speech in future). CARIN will be the subject of a forthcoming article in this journal.

pressure differences that are generated by the human speech-production system (vocal cords, mouth cavity, nasal cavity and pharynx). *Fig. 1* shows an example of a speech sound recording. The mouth and nasal cavities and pharynx (the vocal tract) can be regarded as a resonant cavity that is excited by the periodic vibration of the vocal cords into the voiced elements of speech (e.g. the vowel [a:]) or by turbulences that occur at constrictions in the vocal tract (e.g. the sibilant [s]). This excitation can be characterized by three parameters: the amplitude, which is connected with the loudness of the signal, a parameter that indicates whether the sound is voiced or unvoiced [2] and the source frequency at which the vocal cords vibrate. The resonant cavity can be characterized by the centre frequencies and the bandwidths of the formants, i.e. the resonance peaks in the transfer function. The source frequency is found in the fine structure of the spectrum, the formants in the envelope. The spectrum of speech up to a frequency of 5 kHz usually contains five formants, so that the resonant cavity can be described by ten parameters [2], the five centre frequencies and the corresponding bandwidths.

In principle, synthetic speech can be generated by specifying the behaviour of the thirteen parameters as a function of time. But this requires a large number of complicated rules, some of them as yet unknown. In practice, this approach is difficult and the speech quality is poor.

Another possible way of generating synthetic speech consists in joining together ('concatenating') fragments of natural speech. In its simplest form this amounts to the auditory presentation of *complete messages* spoken-in beforehand, as mentioned before.

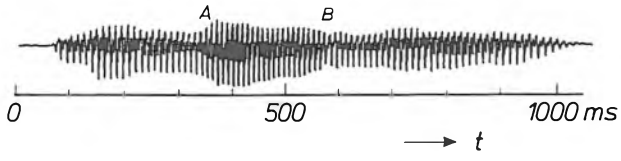


**Fig. 1.** The speech signal, showing the pressure changes as a function of time, for the nonsense word 'nenaanene' spoken by the test subject. At *A* and *B*, for example, the speech signal changes, where there is a transition between two sounds.

More scope is then offered by concatenating *separate words* to form complete sentences. But if all conceivable speech utterances are to be possible with such a system, an enormous list of words will be necessary. We can limit the volume to some extent by using *syllables* instead of words as our basic units. But even then, we still require a quite substantial 'library' of basic units. The library can be reduced to the minimum if we take as our units the smallest segments of speech that still carry differences in meaning, the *phonemes* [3]. To maintain the fluent character of speech, however, it is then necessary to generate the transition from each phoneme to the next by sets of rules that are difficult to establish.

We have no need of such rules if we take *diphones* as our basic units. A diphone is a brief segment of speech that contains the last part of one phoneme, the transition, and the first part of the next phoneme. (*Fig. 2* shows the phonemes and diphones contained in the word 'spoon'.) The number of basic units is now

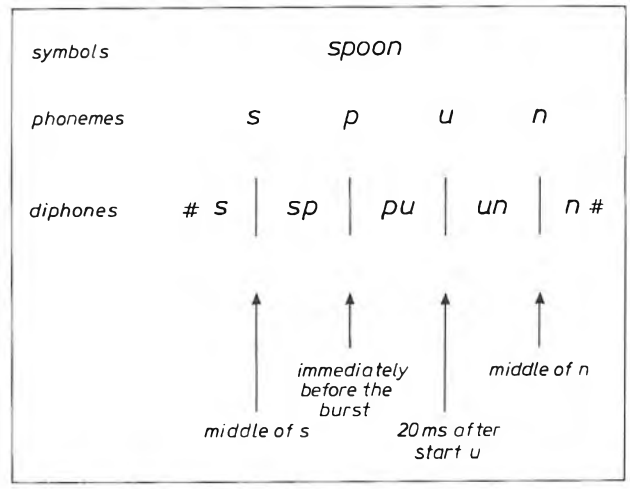


**Fig. 2.** An example of the location of the diphone boundaries in the word 'spoon'. After the phoneme boundaries have been determined, the diphone boundaries are fixed by rules. The first diphone is the transition from silence [ # ] to [s], the next one from [s] to [p], and so on.

larger, but we do not need to add any rules for the transitions. The Dutch language for example contains some forty phonemes. A library of diphones thus consists of some 1600 basic units. For each of these diphones a parameter representation must be available in the speech alphabet. The individual diphones of this library can be joined together to produce words or sentences.

A diphone library can be obtained in the following way. Tape recordings are made of a large number of words, which are spoken by a selected speaker. The list of words is compiled in such a way that it contains all the possible combinations of speech sounds. Four-syllable nonsense words may often be used, such as 'nenaanene' [nəna:nənə] and 'pepaapepe' [pəpa:pəpə], in which the second syllable has to provide the diphones. The procedure is as follows. The words are digitized at a sampling rate of 10 kHz, and then the parameters mentioned above are determined and stored as a continuous series in a memory. This is used for generating (resynthesizing) a new speech signal. The phoneme boundaries are determined from the

parameter values and by listening to the resynthesis. These boundaries are thus established non-automatically. The diphone boundaries are then calculated from the phoneme boundaries, using a set of rules. The rules for positioning the diphone boundaries are different for each phoneme. In vowels the diphone boundary is located at a fixed time after vowel onset. The reason for this is that a vowel in natural speech is not affected, or only slightly, by the consonant immediately preceding it, but it is affected by the consonant immediately following it. The duration of a vowel is thus deterined by the phoneme following the vowel; see for example fig. 2, where the boundary between the [pu] and the [un] diphone is located 20 ms after the start of the [u]. In plosives [b], [d], [p], [t] and [k] the diphone boundary is located immediately before the burst and in all other consonants it is positioned in the middle of the phoneme. These rules are used for determining the diphone boundaries. The parameters between the boundaries are stored in the diphone library.

This non-automatic method of building up a diphone library is tedious and time-consuming. A Dutch diphone library has been prepared in this way for one speaker (B.A.G. Elsendoorn) [4]. The quality of the synthetic speech produced by concatenating diphones from this library is fairly good. There is a need for diphone libraries for more languages and more speakers for each language. (Although there are considerable differences between the diphone libraries for different languages, the principle for the concatenation of diphones can be used for various languages). The procedure described above has to be repeated, however, for each language and for each speaker. This is why efforts have been made to find an automatic method of preparing diphone libraries from recordings of spoken words. Besides the time argument there is a second reason for researching automatic segmentation. An automatic method may be expected to yield a final result that is more easily reproducible and more consistent than that of a non-automatic method.

In the rest of this article we shall consider a number of possible methods of automatic segmentation into phonemes, from which the diphones are then calculated from a set of rules, and it will be shown that a combination of two such methods gives a satisfactory result.

## Automatic segmentation into phonemes

Segmentation methods described in the literature can be classified into two groups. On the one hand there are the methods that look for recognizable features in the speech sound, such as the boundaries between more or less steady-state parts of the speech signal. In the methods of this kind no use is made of the fact that the word to be segmented is known. There is therefore no phonetic identification, that is to say no attempt to link a phoneme with the associated segment of the signal. On the other hand there are methods that make the division on the basis of the correspondence between the speech utterance and a known reference pattern of each sound in the speech utterance. Both methods have their advantages and disadvantages. When a method of the first kind is used the boundaries between the segments are relatively accurately defined, but the segments delimited by two boundaries are not provided with any phonetic identification. A method of the second kind does not in practice appear to meet the requirements imposed by a speech-synthesis system for the accuracy of the boundaries [5]. We shall first consider the method of the first kind that we are using. It will then be shown how satisfactory results can be achieved by combining this method with a method in which use is made of reference patterns.

### *Segmentation into steady-state segments*

In general the behaviour of the acoustic properties of speech sound as a function of time is rather unpredictable. Nevertheless, it is possible to identify 'steady-state' [6] segments of the speech signal, which is usually portrayed in terms of the pressure changes as a function of time. Fig. 1 shows the speech signal of the nonsense word 'nenaanene'. At the points *A* and *B*, for instance, transitions can be seen between two steady-state segments. The transitions are also visible in the spectral composition of the signal at the different times.

---

[2] The sounds are either 'voiced' or 'unvoiced', depending on the vibration of the vocal cords during articulation. All the vowels and the consonants [m], [n], [l], [b], [g] and [d] are voiced, and the plosives [p], [t] and [k] and the fricatives [s] and [f] are unvoiced. See also: J. 't Hart, S. G. Nooteboom, L. L. M. Vogten and L. F. Willems, Manipulation of speech sounds, Philips Tech. Rev. **40**, 134-145, 1982.

[3] In phonetic script phonemes are written as follows: short vowels with the associated letter (e.g. [æ] as in 'mat', [ɔ] as in 'rot' etc.), long vowels with the associated letter plus a colon (e.g. [a:] as in 'father', [ɔ:] as in lawn, etc.), consonants are also represented by the associated letter (e.g. [p] as in 'put', [f] as in 'find' etc.). The a as in 'ago' is indicated by [ə], the 'ur' as in 'turn' by [ə:], [#] indicates silence and [ʔ] the glottal stop. More information about phonetic representation will be found in most bilingual dictionaries.

[4] B. A. G. Elsendoorn and R. J. H. Deliege, A speech synthesis system using diphones: a portable communication aid for the speech impaired, Proc. Eur. Conf. on Technology & Communication Impairment, London 1985.

[5] L. R. Rabiner, A. E. Rosenberg, J. G. Wilpon and T. M. Zampini, A bootstrapping training technique for obtaining demi-syllable reference patterns, J. Acoust. Soc. Am. **71**, 1588-1595, 1982.

[6] These parts of the signal are not truly steady-state. The shape of the curve changes, but not so much as the relative change between the segments.

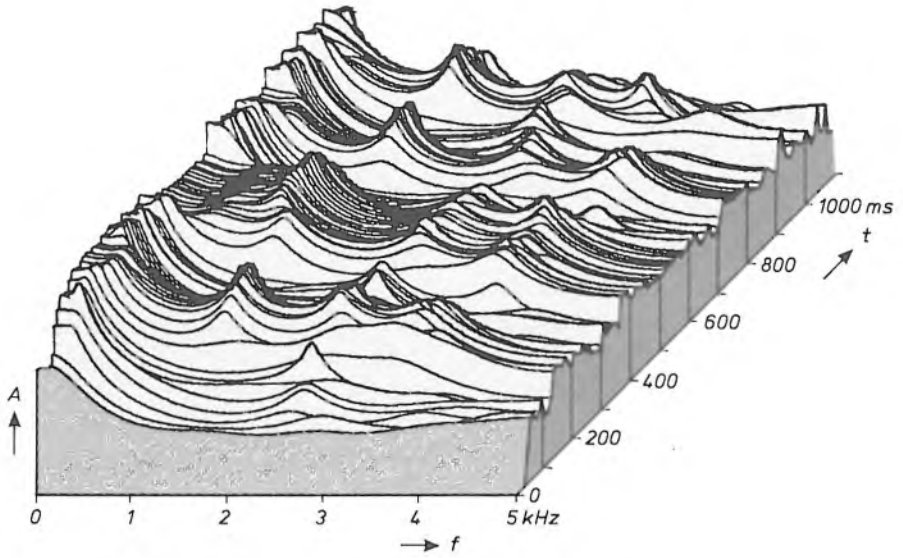


**Fig. 3.** The spectra (the amplitude $A$ as a function of frequency $f$) as determined every 10 ms from the speech signal of the word 'nenaanene'. In most spectra five maxima can be recognized. These are the formants, and their heights and positions vary with time. These signals give the basis for dividing the utterance into steady-state parts.

*Fig. 3* shows a number of 'pictures' of the amplitude spectrum at intervals of 10 ms. The formants, the peaks in the spectra, are subject to changes. The centre frequency and the bandwidth vary with time. With the aid of such a representation, amplitude spectra at intervals of 10 ms, the utterance can be divided into steady-state segments. Two spectra belong to the same steady-state segment of the utterance when they resemble each other to some extent. We must therefore indicate a measure of the similarity between the spectra. To do this we proceed as follows. We determine the extent of the similarity between two spectra by calculating the correlation between them. This correlation $c_{i,j}$ is defined as:

$$c_{i,j} = \frac{(s_i \cdot s_j)}{\sqrt{(s_i \cdot s_i)(s_j \cdot s_j)}}, \qquad (1)$$

where $(s_i \cdot s_j) = \int_0^{5\,\mathrm{kHz}} W(f) s_i(f) s_j(f) \mathrm{d}f$, the scalar product of the spectra $s_i$ and $s_j$, where $f$ is the frequency and $W(f)$ the spectral weighting function that approximates to the sensitivity of the human ear. This spectral weighting function is given by:

$$W(f) = \begin{cases} 0 \text{ if } 0 < f \leqslant 200 \text{ Hz} \\ 1 \text{ if } 200 < f \leqslant 1000 \text{ Hz} \\ \dfrac{1000}{f} \text{ if } f > 1000 \text{ Hz}. \end{cases}$$

If two spectra are identical, the correlation $c_{i,j}$ is equal to 1. But as the similarity of the spectra diminishes, the more $c_{i,j}$ will differ from 1. The correlation $c_{i,j}$ between the $i$th spectrum and the ten neighbours on both sides ($i - 10 \leqslant j \leqslant i + 10$) is shown schematically in *fig. 4*. The curve has a maximum 1 at $j = i$. After choosing a threshold value $c_t$ we can identify a segment belonging to spectrum $i$ as the series of successive spectra (from $i_b$ to $i_e$) whose correlation with spectrum $i$ is greater than the threshold value $c_t$. The boundary between two segments is established in the following way. For all segments we determine the 'centre of mass' $m_i$, which is defined as:

$$m_i = \frac{\sum_{j=i_b}^{i_e} j(c_{i,j} - c_t)}{\sum_{j=i_b}^{i_e} (c_{i,j} - c_t)}. \qquad (2)$$

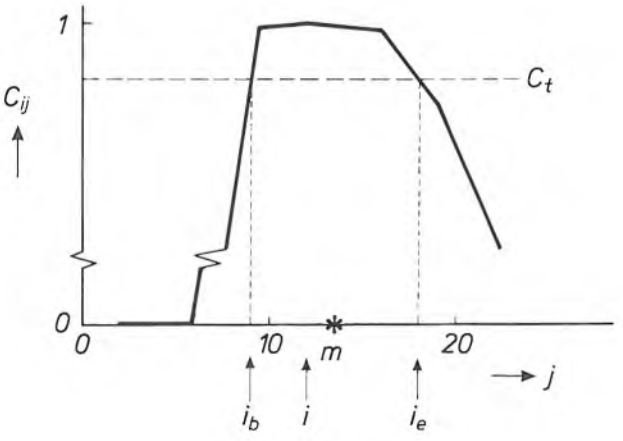


**Fig. 4.** Diagram representing the correlation $c_{i,j}$, the correlation between the spectra of the $i$th (= 12) spectrum and the $j$th spectrum ($j$ goes from 2 to 22). The $i$th and the $j$th spectra belong to the same steady-state segment of the speech utterance if the correlation between the corresponding spectra is greater than $c_t$. In this schematic example the spectra $j = 9$ (= $i_b$) to $j = 18$ (= $i_e$) belong to the same steady-state segment. The 'centre of mass' $m_i$ (see text) is also indicated in the figure.

The distance $d_i$ from spectrum $i$ to the centre of mass $m_i$ of a segment is used for establishing the boundaries: $d_i = m_i - i$. Exactly how this is done can be seen by referring to the example given in *fig. 5*. For our nonsense word 'nenaanene' we have a representation of the speech signal, the correlations $c_{i,j}$ between the spectra, and the distance function $d_i$. For all $i$, the curve $c_{i,j}$ gives the correlation between spectrum $i$ and the other spectra $j$ in this speech utterance. From $i = 14$ to $i = 24$ the correlation curve changes only slightly. Near $i = 25$ we find a transition, and then the maximum of $c_{i,j}$ moves to larger $j$-values. The centre of mass of the curve is indicated by a short vertical line. The short horizontal lines indicate the distance $d_i$ from spectrum $i$ to the centre of mass $m_i$ of the correlation curve. This distance is also plotted at the bottom of the figure. The zero crossings of the distance function from plus to minus are all close to the centre of a steady-state segment. The zero crossings from minus to plus are close to a transition, and are taken as the boundaries between two steady-state segments.

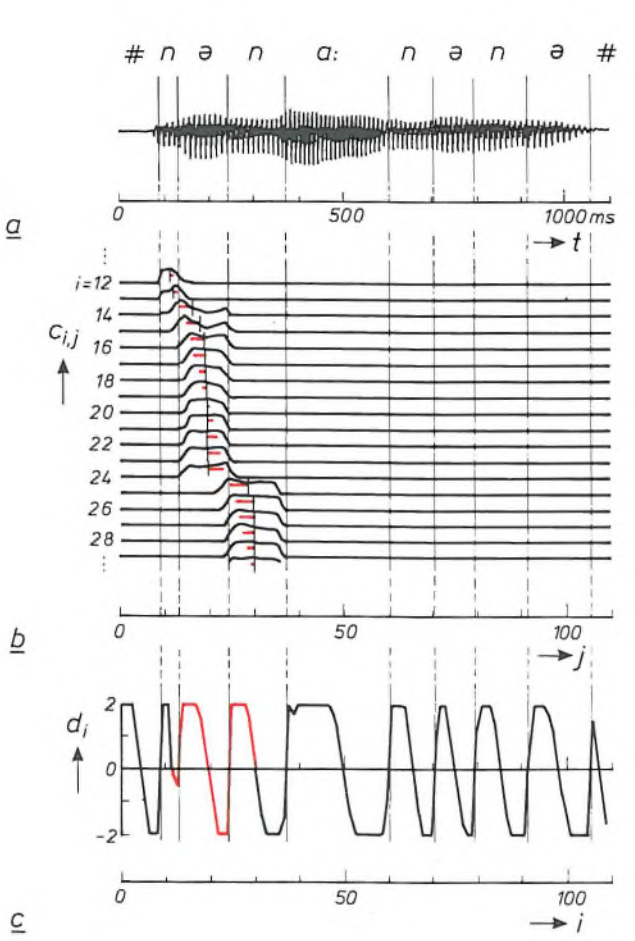


**Fig. 5.** The speech signal (*a*), the correlation $c_{i,j}$ for a part of the speech signal (*b*) and the distance function $d_i$ (*c*) derived from the correlation. The lines indicating the phoneme boundaries derived from the zero crossings (from − to +) of the distance function are extended to the speech signal.

The $n$th boundary determined by this method is called $g_{1,n}$. We shall return to this later.

Phoneme boundaries have been determined in this way for a number of nonsense words. A comparison of these results with results obtained non-automatically shows that the phoneme boundaries have been fairly accurately determined. It can happen, however, that some boundaries are not found or that a phoneme is divided incorrectly into more than one segment. The number of incorrectly determined boundaries is so small, however, that this method can be used in an automatic segmentation program. For our real purpose, the segmentation into diphones, however, we do have to know which segments and phonemes correspond. In the following subsections we shall see how segments are given their phonetic identification. We shall also consider which boundaries have to be ignored or included to obtain the correct number of phonemes in an utterance.

### *Segmentation with the aid of reference patterns*

In the division into steady-state segments as discussed in the previous subsection, we did not establish which steady-state segments and phonemes correspond. We do however know how many phonemes there are in the word to be segmented, and which ones they are. We can use this information to identify the steady-state segments. This can be done, for instance, by connecting the successive steady-state segments with the phonemes in the sequence occurring in the word to be segmented. This does not always work, however. There are some phonemes, the diphthongs (e.g. [ei], [ou], [ai]) and the plosives (e.g. [b], [d], [t]), that consist of two more or less steady-state sections. Furthermore, errors can be introduced by determining too many boundaries or too few. It is therefore necessary to ascertain whether the spectra of a steady-state part of the utterance do indeed correspond to the spectra of the intended phoneme. The procedure we follow for this is now described.

The word to be segmented is split into 'spectral states'. Most phonemes correspond to one spectral state; only the diphthongs and plosives correspond to two spectral states. We characterize each spectral state by a spectrum that we obtain from a series of spectra corresponding to the phoneme. We shall call these spectra the reference spectra. Next we compare the spectra of the speech utterance (we shall call these the test spectra) with the reference spectra of all the states that occur in the speech utterance. We do this in the same way as described in the previous subsection, by determining the correlation between the reference spectra and the test spectra. Let us illustrate this by an example. The word 'nenaanene' mentioned earlier

contains ten spectral states: the silence before the word [ # ], the phonemes [n], [ə], [n], [a:], [n], [ə], [n], [ə] and the silence after the word [ # ].

*Fig. 6* shows the reference spectrum $n$ for each of these spectral states and the correlation $c_{i,n}$ of all the test spectra $i$ with the different reference spectra. The correlation is high if the test spectra closely resemble the reference spectra. The correlation of all the test

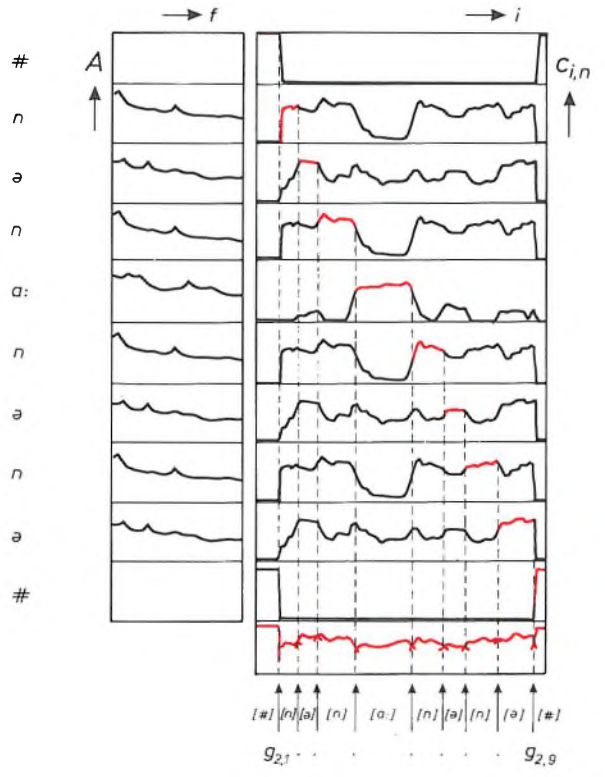


**Fig. 6.** The spectral states, the associated reference spectra $n$ and the correlation $c_{i,j}$ between the reference spectra and the test spectra in the word 'nenaanene'. The arrows below indicate the boundaries $g_{2,n}$, as determined subject to the condition that the total sum of the correlations between the boundaries must be as large as possible. $A$ is the amplitude, $i$ the test spectrum and $f$ the frequency.

spectra $i$ with a reference spectrum $n$ shows — depending on the number of times the spectral state occurs — a number of regions where the correlation is high. The correlation curve of the reference spectrum of the [n], for example, has four such regions, one for each occurence of the [n] in the word. In principle, this spectral information can be used as the basis for segmenting an utterance. The spectral variability of speech is so great, however, that the correlation between the test spectra and a reference spectrum can always be lower than the correlation with other reference spectra, which would give the corresponding spectral state a zero duration. To prevent this, restrictions are imposed on the duration of each spectral state. The minimum and maximum durations of each spectral state are estimated by measuring the duration of a number of 'realizations' of that state.

We can now formulate a rule for the segmentation. The word to be segmented contains $N$ spectral states and is available in the form of $I$ test spectra. The last test spectrum associated with the $n$th spectral state we call $g_n$. The boundaries $g_n$ for $n = 1$ to $(N-1)$ are the free parameters that have to be determined. The boundary $g_0$ is set at the start of the speech utterance and the boundary $g_N$ is set at the end: $g_0 = 0$ and $g_N = I$. The free parameters have to be determined in such a way that the resemblance between reference and test spectra is as close as possible, subject to the condition that the duration of each spectral state must lie between the associated minimum and maximum values ($\min_n$ and $\max_n$). This requirement is formulated as:

$$\max_{g_n} \sum_{n=1}^{N} \sum_{i=g_{n-1}+1}^{g_n} c_{i,n}, \qquad (4)$$

with the condition $\min_n \leqslant g_n - g_{n-1} \leqslant \max_n$. This maximization can be performed by 'dynamic programming' [7]. The results of these calculations can be found in the last graph of fig. 6. This shows parts of the correlation curves between the boundaries calculated as described above. The spectral state is also shown. In general, the inaccuracy in the determination of the boundaries by this method is too great for our purpose (see also fig. 10). In the next section we shall see that this method can however be used for generating the phonetic identification for the segments with steady-state properties, as obtained by the method described in the previous section.

### *Combination of the two methods of segmentation*

*Table I* shows the advantages and disadvantages of the two automatic segmentation methods discussed earlier. It can be seen that the methods are more or less complementary. It is therefore logical to combine the two methods in such a way as to retain the advantages of each and avoid the disadvantages. This can be done by using the determination of the segment boundaries of the first method (which is accurate) and the phonetic identification of the second method. For

**Table I.** The advantages and disadvantages of the two automatic segmentation programs.

| | Advantages | Disadvantages |
|---|---|---|
| First method | accurate determination of boundaries | too few boundaries or too many<br>phonetic identification not known |
| Second method | correct number of boundaries<br>phonetic identification known | boundaries not accurately determined |

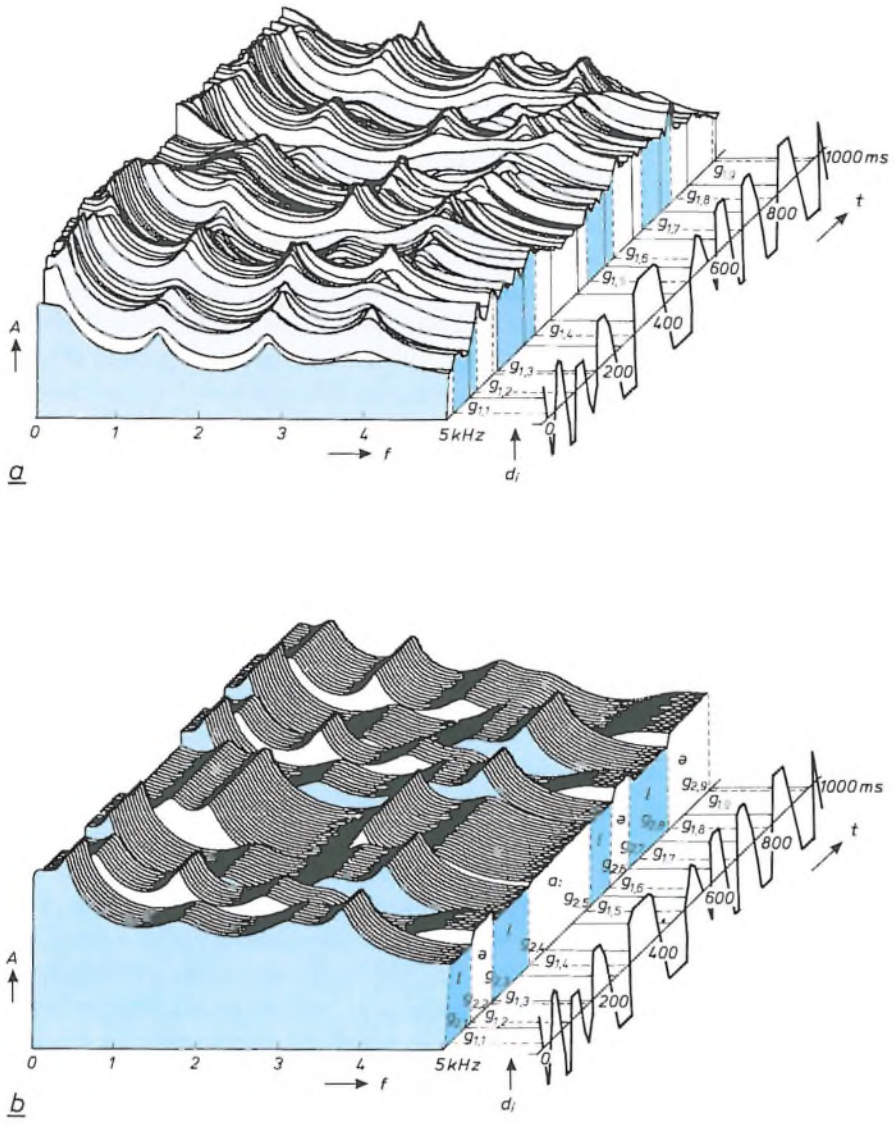


**Fig. 7** *a*) The spectra of the word 'lelaalele' (the amplitude $A$ as a function of frequency $f$ at successive times). Segmentation into steady-state parts is done with the aid of the distance function $d_i$ (equations 1, 2 and 3). The distance function $d_i$ and the boundaries $g_{1,1}$ to $g_{1,9}$ derived from it are shown along the time axis. *b*) The boundaries $g_{2,1}$ to $g_{2,9}$ are found with the second automatic segmentation method. The diagram shows, between two boundaries, the reference spectra with which the spectra give the maximum correlation at the associated times (equation 4). Simply placing these reference spectra in sequence gives a picture (and also a sound) that is different from that of (*a*). The distance function $d_i$ and the boundaries $g_{1,1}$ to $g_{1,9}$ derived from it are also indicated. The boundaries determined by the two methods do not correspond with one another everywhere.

this we need an algorithm that combines the boundaries determined by both methods. This implies that any extra boundaries found by the first method are omitted, and that any boundaries not found are inserted.

*Fig. 7* shows the results of both methods once again. Fig. 7*a* gives the spectra of the nonsense word 'lelaalele' [ləla:lələ]. The distance function $d_i$ is shown along the time axis, with the boundaries $g_{1,n}$ derived from it (first method). The boundaries determined by the second method ($g_{2,n}$) can be seen in fig. 7*b*. This figure only gives the reference spectra that we used for determining these boundaries. Note that there is a considerable difference between the actual spectra (fig. 7*a*) and the steady-state 'caricature' of them obtained by the second method (fig. 7*b*). The distance function $d_i$ and the boundaries $g_{1,n}$ derived from it are again shown along the time axis. At some places the boundaries $g_{1,n}$ and $g_{2,n}$ are different. The boundaries closest to one another, $g_{1,n}$ and $g_{2,n}$, are linked. The final location of the boundaries is derived from the first method and the phonetic identification from the second method. A diagrammatic representation of this procedure is given in *fig. 8*. The link between two boundaries is represented as a dashed line. The linking of the boundaries can be continued until a number of boundaries remain that cannot be linked without the dashed lines crossing. The dashed lines must not

[7] 'Dynamic programming' is a mathematical procedure for solving an optimization problem. The solution is reached in different stages, in each of which a number of decisions can be made. The method can be efficiently programmed. More information can be found in books such as:
O. I. Elgerd, Control systems theory, McGraw-Hill, New York 1967;
R. E. Bellman, Dynamic programming, Univ. Press, Princeton, NJ, 1957.

cross because the sequence in which the segments have to be found is fixed. The boundaries $g_{1,n}$ that cannot be linked are omitted. The boundaries $g_{2,n}$ that cannot be linked are retained. The final location of these boundaries is derived from the second method. In the other cases, in which the boundaries can be linked, the final location of the boundaries is derived from the first method.

*Fig. 9* shows an example of the segmentation obtained with the two methods combined, showing the boundaries ultimately established in the speech signal.

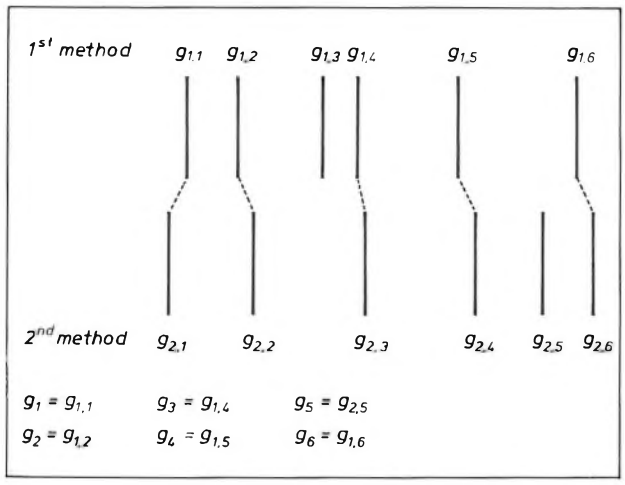


**Fig. 8.** A stylized example of the algorithm that combines the boundaries found by the two automatic segmentation methods. The upper vertical lines indicate the boundaries found by the segmentation into steady-state segments ($g_{1,1}$ to $g_{1,6}$) and the lower vertical lines give the results of the reference method ($g_{2,1}$ to $g_{2,6}$). The boundaries are linked by dashed lines in such a way that the total length of all the dashed lines has the minimum value. The dashed lines must not cross. The final results for the phoneme boundaries are also shown.

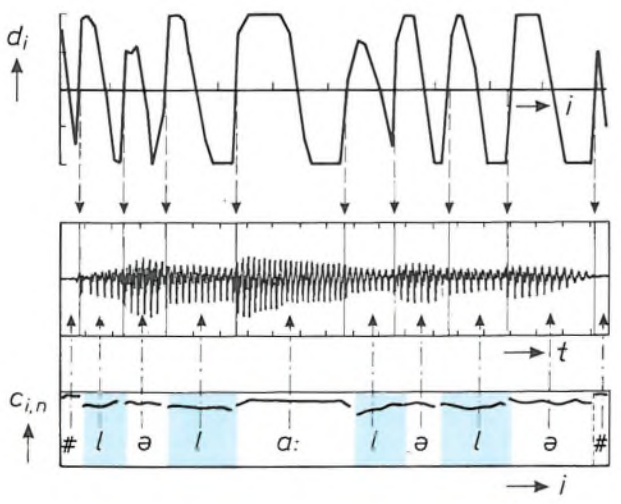


**Fig. 9.** The distance function $d_i$, the speech signal and the correlation $c_{i,n}$ between the spectral states [#], [l], [ə], [l], [a:], [l], [ə], [l], [ə], [#] and the spectra for the word 'lelaalele'. The phoneme boundaries finally determined are shown in the speech signal.

## Synthetic speech built up from diphones

The methods discussed above have been programmed on a VAX 11/780 computer. These programs have been used to make diphone libraries for Dutch, German and British English. The diphones are stored in parametrized form in these libraries. All possible speech utterances can be made audible by retrieving the appropriate diphones from the library, concatenating and synthesizing them. An example will be given to illustrate the final result. *Fig. 10* shows the behaviour of the parameters as a function of time for the simple sentence 'The sun rises.' The parameter values of the diphones are shown in sequence. To make the synthetic speech more natural the source frequency is added by means of a set of rules [8]. In this example the stress is on the word 'sun'. At the boundaries between the diphones (vertical dashed lines) there are occasional discontinuities. These are not usually audible in the synthesis made by means of this parametrization. Before considering the result of an evaluation made by subjects who listened to a number of such synthesized utterances, we shall first look at a comparison of phoneme boundaries obtained by automatic and non-automatic means.

The phoneme boundaries of a number of words were determined by the usual non-automatic method, the second method and the two automatic methods combined. The results of these determinations are compared in *fig. 11*. The figure shows the percentage of phoneme boundaries for which the difference between the automatically and non-automatically determined boundaries is less than or equal to a particular multiple of 10 ms (the time interval between two spectra). Assuming that the non-automatically determined boundaries are somewhere near what we need for our purpose, we find that the results obtained by combining the two automatic methods give a definite improvement. If the required accuracy is set at 30 ms, 96% of all phoneme boundaries are correctly determined.

The agreement between automatically and non-automatically determined phoneme boundaries does not in itself show that the library of diphones obtained automatically is useful in practice for generating synthetic speech. Information about this can be obtained by asking subjects to assess the intelligibility and quality of the synthetic speech. A Dutch-language version of a diphone library has been used for this perceptual evaluation. Constant-pitch syntheses were therefore made of 320 words of one or two syllables from both the 'automatic' and the 'non-automatic' diphone libraries. Syntheses of both types were played in random order to seven subjects, who were asked

[8] J. 't Hart and R. Collier, Integrating different levels of intonation analysis, J. Phonet. 3, 235-255, 1975.

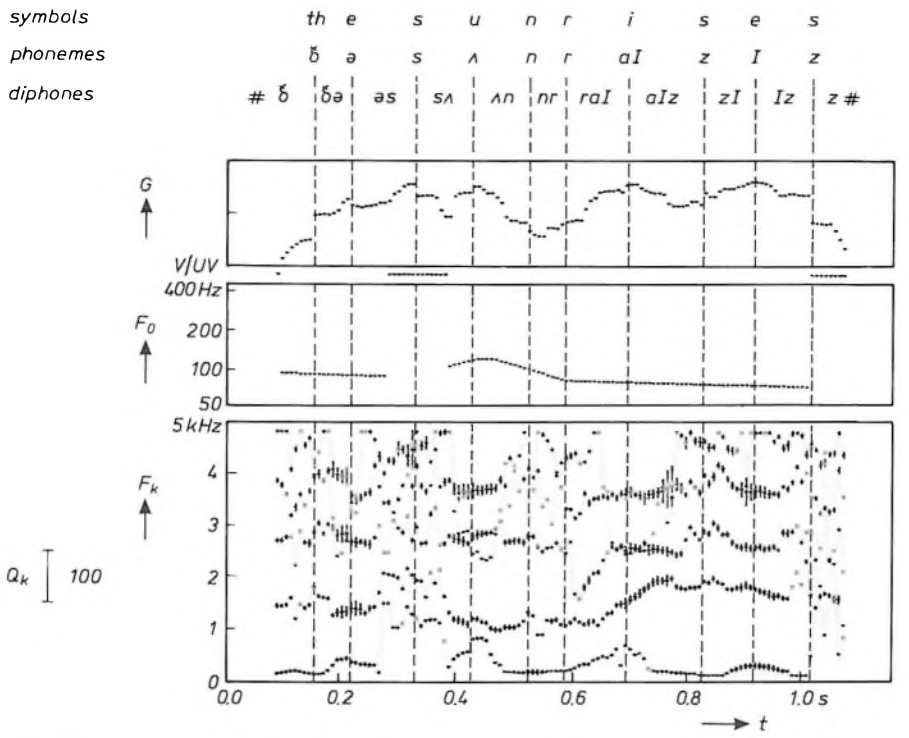


**Fig. 10.** Example of a concatenation of diphone parametrizations from the 'automatic' diphone library. From top to bottom: the sentence 'The sun rises.', the corresponding phonemes, the corresponding diphones, the mean amplitude $G$ of the speech signal, the value of $V/UV$ — unvoiced is shown black, voiced white — the source frequency $F_0$ in the voiced parts of the sentence, the centre frequency $F_k$ and the $Q$ (quality factor) $Q_k$ ($k = 1$ to 5) of the five formants that characterize the resonant cavity. The centre frequency is indicated by a horizontal dash. The $Q$, which is inversely proportional to the bandwidth, is indicated by a vertical dash through the corresponding value of $F_k$. The value of the source frequency does not depend on the concatenation of the diphone parametrizations but has been added. The vertical dashed lines indicate the boundaries between the successive diphones.

which word they had heard. The subjects could also evaluate the quality of the synthetic speech by awarding points. The scores are presented in *Table II*. It can be seen that the 'automatic' diphone library is certainly no worse than the 'non-automatic' one. Although this does not prove that the automatic segmentation always gives better results, it does show that 'automatic' diphone libraries can compete well with 'non-automatic' ones. In view of the other advantages, automatic segmentation is preferable to non-automatic segmentation. The fact that words are misunderstood in an intelligibility test is not solely attributable to erroneous segmentation of speech into diphones, of

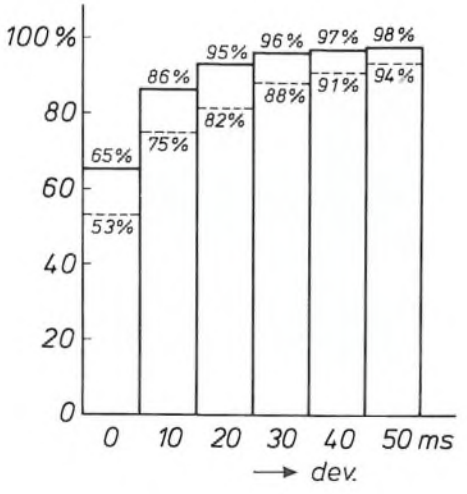


**Fig. 11.** The percentage of 'automatic' phoneme boundaries that deviate by less than an indicated multiple of 10 ms from the 'non-automatic' phoneme boundaries. The dashed lines with the corresponding percentages indicate the results of the second method, the continuous lines give the results of the combination of the two methods. In total 979 phonemes boundaries were determined in 90 words.

**Table II.** Results of the perceptual evaluation. Altogether 320 words were synthesized from both the 'automatic' and the 'non-automatic' libraries. Seven test subjects were asked to identify the spoken word. The subjects were also able to give their evaluation of speech quality.

| | Diphone set | |
|---|---|---|
| | 'automatic' | 'non-automatic' |
| Percentage of words wrongly understood by everyone | 2% | 3% |
| Percentage of words wrongly understood by at least one person | 29% | 35% |
| Total percentage of wrong scores (100% corresponds to 7 × 320 words) | 9.5% | 12.5% |

course. Errors of analysis, the way in which the syntheses are made, the nature of the equipment, discontinuities and other factors all come into the picture.

The evaluation of the quality of the speech by different subjects is difficult to bring to a common denominator because their judgement is subjective. It can however be concluded that six of the seven subjects considered the quality of the syntheses made with the 'automatic' diphone library to be better than that of the syntheses made with the 'non-automatic' diphone library.

One aim of the investigation, to shorten the time it takes to prepare a diphone library from which synthetic speech of good quality can be produced, has been achieved. The segmentation of the speech utterances into diphones, which is a part of the process, can now be done in a fraction of the time that a 'non-automatic' method would have required. Synthetic speech built up from diphones obtained in this way will in future be subjected to further perceptual evaluation. An effort will also be made to improve various details of the method. The strategy described can be used to build up a diphone library in less time than before. The availability of high-quality diphone libraries for more speakers and more languages could in future lead to promising applications, such as multilingual talking dictionaries and dialogue systems.

**Summary.** Systems in which synthetic speech is generated often use a library of sound transitions (diphones) as units for forming words in the same way as the letters of the alphabet are used for writing. The libraries are built up by extracting these units from spoken text. This can be done automatically by a combination of two automatic methods. In the first method, boundaries can be placed in words at positions where one steady state changes into another one. In the second method the sounds in a word are compared with reference patterns of particular sounds, and the phonetic identification is assigned to the segments determined by the first method. The second method is also used for correction if too many boundaries or too few are found. The boundaries obtained in this way are not very different from the results obtained by non-automatic methods. With these methods diphone libraries can be built up in a fraction of the time that would be required with a non-automatic method. Evaluation by test subjects of synthetic speech built up from 'automatic' diphone libraries is certainly no worse than that of synthetic speech built up from 'non-automatic' diphone libraries.

# 1937 THEN AND NOW 1987

## Transmitting valves

Fifty years ago the TA 20/250 transmitting triode was the largest transmitting valve in the Philips production range; see the photograph at the upper right [*]. This valve was 1.40 m high, and could supply a continuous-wave output power of 65 kW or a peak pulse power of 260 kW. The electrode system in this type of transmitting valve took the form of concentric cylinders, with the cathode at the centre and the anode at the outside. The heat dissipation was greatest at the anode, which was therefore force-cooled by a current of water.

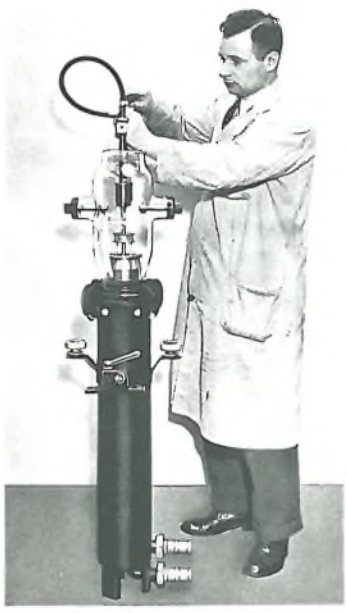

The TA 20/250 transmitting triode was used in long-wave broadcast transmitters, since the valve could only be used at relatively low frequencies (1 MHz and below) because there was glass insulation between the electrode connections and the electrode system was relatively long. (The length of the electrodes should be small compared with the wavelength of the transmitted signal.) The water-cooled anode could dissipate a maximum of 100 W/cm$^2$.

Triodes that will provide very high powers are still produced today, and their construction remains very much the same. The largest type in the present range has a continuous-wave output power of 500 kW and a peak pulse power of 2 MW. The height of this valve is 0.80 m; see the valve at the back in the lower photograph. The heat transfer has been greatly improved, so that the length of the electrode system need only be less than half that of the TA 20/250 transmitting triode of 1937. This and the ceramic insulation with very low dielectric losses make these valves useful at considerably higher frequencies, so that they can be used — in tetrode form — in short-wave broadcast transmitters at frequencies up to 30 MHz. As triodes they are also used for heating plasmas in controlled nuclear fusion. The frequency of about 100 MHz then used is equal to the cyclotron frequency of the ions in the plasma.

The two valves at the centre of the lower photograph are air-cooled, the other three are water-cooled. Because the water cooling is very efficient the anode can dissipate a maximum of about 1000 W/cm$^2$. The high heat transfer has been achieved by the use of special grooves on the outside of the anode.

[*] From Philips Technical Review, April 1937.

Philips Tech. Rev. 43, No. 9, 244-252, Sept. 1987

# Black-cobalt coating for solar collectors

B. Vitt

*The efficiency of a solar collector can be improved considerably by using an absorber plate with a black-cobalt coating which is spectrally selective. Until recently, making suitable coatings was mainly an empirical process. The article below describes an investigation into the fundamental properties of such coatings. The results can be used successfully to optimize coatings for high-temperature applications.*

## Introduction

In a solar collector, an absorber plate with a black coating is used to convert the solar energy into thermal energy. The heat collected is transferred to a circulating medium (e.g. water or oil) and can be used for a variety of purposes, e.g. for space heating or in industrial processes. Various measures can be taken to compensate for the increase in thermal radiation losses at the plate when it is operating above ambient temperature. These include a concentration of the solar energy by reflectors and lenses, and a reduction of convection and conduction losses by evacuation of the collector tube. The efficiency of the energy conversion can be improved further by using a spectrally selective black coating which has a high absorptance for solar radiation, i.e. at wavelengths shorter than about 2.5 μm, and a small emissivity for thermal radiation at longer wavelengths.

Several materials have been investigated for this application [1]. As a part of the Philips activities on evacuated solar collectors [2] an efficient black-cobalt coating was developed in our laboratories. An electroplating process was used to successfully apply this to the inside walls of silver-coated glass tubes in an experimental collector [2] [3]. Later on, a quantity-production process was developed at the Philips Plastics and Metalware Factories in Eindhoven for deposition on copper-coated steel plates. These were used in the commercial Philips evacuated tubular collector, in which the heat gained by the absorber is extracted efficiently via a heat pipe [4].

*Dr B. Vitt is with Philips GmbH Forschungslaboratorium Aachen, Aachen, West Germany.*

The efficiency and life of a solar collector depend strongly on the selective properties and stability of the black coating. In the vacuum environment of an evacuated tube there is no stability problem as long as the collector is designed for 'load' temperatures no higher than 150 °C. However, in view of the good selective properties of cobalt coatings a modification of the collector design seems to be possible in a way that allows efficient production of process heat in the high-temperature range of 150 to 250 °C [5]. In this case stagnation temperatures of more than 350 °C can arise, requiring extended knowledge of the long-term stability of the coating under such conditions.

During our investigations cobalt coatings were deposited on various steel substrates. The samples were characterized chemically and optically, with emphasis on the stability properties at elevated temperatures in various atmospheres [6]. In addition, the effect of the substrate on the optical properties and stability was investigated. The results have been related to the collector performance. It was found that coatings well-suited for high-temperature applications can be obtained on smooth substrates, after sufficient annealing and outgassing in an inert atmosphere.

In this article we first deal with the structure and chemical composition of the coatings. Next we shall

discuss their optical properties and their behaviour in non-inert atmospheres. Finally we shall show how the coating properties affect the collector performance.

### Structure and composition

For the investigations on the structure and composition black-cobalt coatings were prepared on different steel substrates previously coated with a thin infrared reflecting copper film. The substrates are designated as smooth, medium or rough, corresponding to surface roughnesses of less than 0.05, 0.1 or 1 μm, respectively. The electroplating was carried out at room temperature with a solution containing 25 g/l of cobalt chloride ($CoCl_2$) and 25 g/l of potassium thiocyanate (KSCN), at a pH-value of 4.5. The current density was 1 A/dm$^2$ and the electrolytic thickness of the deposit, expressed as the charge transferred per dm$^2$, was varied up to 500 C/dm$^2$.

The structures of the deposits were characterized by scanning electron microscopy (SEM) as well as by transmission electron microscopy (TEM) for samples which had been made sufficiently transparent to electrons. Like similar electrolytic coatings, the deposits exhibit a rather inhomogeneous and porous structure, depending on the deposition conditions and the roughness of the substrate. SEM micrographs of two coatings on substrates with different roughness are shown in *fig. 1*. The nucleation conditions on the smooth substrate obviously lead to a denser and more compact deposit.

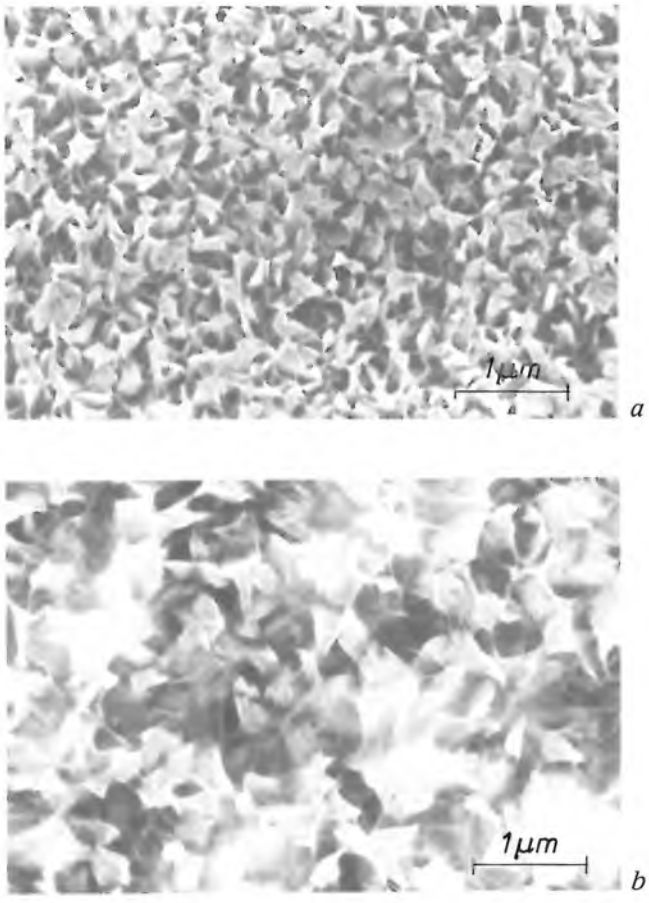


**Fig. 1.** SEM micrographs showing that a cobalt coating of 30 C/dm$^2$ on a smooth substrate (*a*) is much denser than that on a rough substrate (*b*).

Annealing at 350 °C and 450 °C introduces a significant change in the surface structure, and this is accompanied by a decrease in the coating thickness. This decrease amounts to 25% after the 450 °C step and is related to a partial decomposition and to the observed emission of considerable amounts of $H_2O$ and $CO_2$. In addition to showing that the structure is inhomogeneous, TEM micrographs indicate that the material itself is built up inhomogeneously from a granular distribution of particles in a solid matrix of filling material. The particles seem to vary in size from 2 to 10 nm.

Coating material removed from the substrate was found to be ferromagnetic. This indicates the presence of a cobalt-rich phase, since common cobalt compounds such as oxides and sulphides are paramagnetic. This interpretation is supported by energy-dispersive X-ray fluorescence analysis during SEM and TEM, giving an average atomic cobalt/sulphur ratio of 10:1. Infrared reflection spectra reveal the presence of $OH^-$ and $CO_3^{2-}$ ions, pointing to a significant amount of $Co(OH)_2$ and $CoCO_3$. X-ray diffraction does not show any detectable lines, so the deposits are either amorphous or polycrystalline with very small particle sizes. However, after inert annealing at 250 °C diffraction lines of crystalline CoO are obtained. These lines are intensified on annealing in air. For some samples that were annealed at 350 °C the formation of $Co_6S_5$ was detected.

These observations were correlated with a quantitative chemical analysis of coatings of maximum thickness of about 10 μm. The percentages by weight obtained for the elements Co, S, O, C and H were con-

[1] See for example O. P. Agnihotri and B. K. Gupta, Solar selective surfaces, Wiley, New York 1981.
[2] H. Hörster (ed.), Wege zum energiesparenden Wohnhaus, Philips Fachbuchverlag, Hamburg 1980;
H. O. Jungk and H. Scholz, Deutsche Offenlegungsschrift P 25567162;
H. Bloem, J. C. de Grijs and R. L. C. de Vaan, An evacuated tubular solar collector incorporating a heat pipe, Philips Tech. Rev. **40**, 181-191, 1982.
[3] K. R. Schreitmüller and K. Vanoli, Proc. 8th Biennal Congr. Int. Sol. Energy Soc., Perth 1983, pp. 816-824.
[4] J. C. de Grijs and R. J. H. Jetten, Proc. 8th Biennal Congr. Int. Sol. Energy Soc., Perth 1983, pp. 1071-1076.
[5] B. Vitt, Solar systems with highly efficient collectors, Proc. Summer School on Solar Energy, Igls (Austria) 1985, pp. 55-61.
[6] B. Vitt, Characterization of a solar selective black coating, Sol. Energy Mater. **13**, 323-350, 1986.

Table I. Composition of a black-cobalt coating before and after inert annealing at 450 °C. For simplicity the cobalt-sulphur compound is shown as CoS.

| Element or compound | Mol.% | |
|---|---|---|
| | Before annealing | After annealing |
| Co | 62.7 | 63 |
| CoS | 9.6 | 10 |
| $Co(OH)_2$ | 18.8 | — |
| $CoCO_3$ | 8.3 | — |
| CoO | — | 27 |
| Residue | 0.6 | — |

verted into molecular ratios, as given in *Table I*. In view of the TEM results and the ferromagnetic properties it is unlikely that the composition given corresponds to a homogeneous alloy. From energy-dispersive X-ray fluorescence analysis it can be shown that the spatial distributions of Co and S are highly correlated. An inhomogeneous model may therefore be more reasonable, which accounts for a granular distribution of small $Co_{10}S$ particles in a matrix mainly consisting of the 'filling materials' $Co(OH)_2$ and $CoCO_3$.

As would be expected, $Co(OH)_2$ and $CoCO_3$ decompose on annealing in an inert atmosphere, leading to the formation of CoO and the emission of $H_2O$ or $CO_2$. The emission of some CO, $H_2$, $H_2S$ and $SO_2$ may also become significant at higher temperatures. However, the decay of the sulphur content in the samples is very limited below 450 °C. These results show that the coatings should be carefully outgassed at 450 °C before using them in vacuum collector tubes. Table I gives the approximate composition after such a heat treatment. Vacuum annealing at even higher temperatures should then result in a porous layer consisting of cobalt metal plus some mol.% of CoO.

## Optical properties

An important quantity in characterizing an absorber plate for solar collectors is the 'solar absorptance' $\alpha$, which is defined as the fraction of the incident solar power absorbed by the plate. Another important quantity is the thermal emissivity $\varepsilon$, which is the radiated power density divided by the power density radiated by an ideal black surface at the same temperature. To obtain solar collectors with a high efficiency, $\alpha$ should be as large as possible and $\varepsilon$ as small as possible.

These properties were evaluated for coatings of different thickness by measuring the reflection spectra in the infrared wavelength range (2.5 - 50 μm) and in the solar wavelength range (0.3 - 2.5 μm). *Fig. 2* shows the spectra for coatings on smooth steel substrates on which 1 μm of copper had been electroplated from a cyanide solution. The spectra exhibit pronounced interference structures, which shift towards the infrared with increasing thickness. Analysis of the maxima and minima reveals that the geometrical thickness is proportional to the plating time or the electrolytic thickness. This holds at least as far as the 500 C/dm² sample, for which a geometrical thickness of 10 ± 1 μm was determined by microscopy. The spectra also demonstrate that the requirements of a high absorptance in the solar wavelength range and of a high infrared reflectance (low thermal emissivity) are only met by coatings with an electrolytic thickness not exceeding about 30 C/dm².

The spectra of fig. 2 can be described by using unique wavelength-dependent functions for both the refractive index $n$ and the absorption index $k$. Computer simulations were found to fit the measured spectra very well, except for short wavelengths ($\lambda \leqslant 0.8$ μm) and for the vibrational $OH^-$ and $CO_3^{2-}$ peaks [7]. The appropriate optical functions are shown in *fig. 3*. Whereas $n$ increases monotonically with $\lambda$, $k$ decreases from the high value at short wavelengths. However, in the infrared there is an increase in $k$, which is almost the same as the increase in $n$, indicating some metallic behaviour. This increase in $k$ implies that thick coatings are not transparent in the infrared (see also fig. 2). In spite of the combination with a reflecting metal film, a thick black-cobalt film is therefore more like a blackbody radiator than a selective radiator.

The $n$ and $k$ functions also provide a fairly satisfactory description of the directional thermal emissivity $\varepsilon_\phi$, obtained by radiometric measurements of the heat emitted at different values of the angle $\phi$ with respect to the normal to the surface. If $\varepsilon_\phi$ is expressed as a function of $\sin^2\phi$, an expression for the hemispherical emissivity $\varepsilon_h$ can easily be derived:

$$\varepsilon_h = \int_0^1 \varepsilon_\phi \, d(\sin^2\phi).$$

Results for coatings at 127 °C are shown in *fig. 4*. It can be seen that the coating thickness is the most important parameter for the directional emissivity. For thicker coatings the shape of the curve for $\varepsilon_\phi$ differs increasingly from the shape for the uncoated copper surface. The ratio $\varepsilon_h/\varepsilon_\perp$ of the hemispherical emissivity to the emissivity along the normal first increases from the value of 1.3 for uncoated copper to a maximum of about 1.9 and then decreases to values close to 1. The increase in the high-angle emission with very thin coatings is due to the increased optical pathlength at higher angles. For coatings of 60 C/dm² or more the emission characteristics of a weakly absorbing dielectric [8] are obtained.

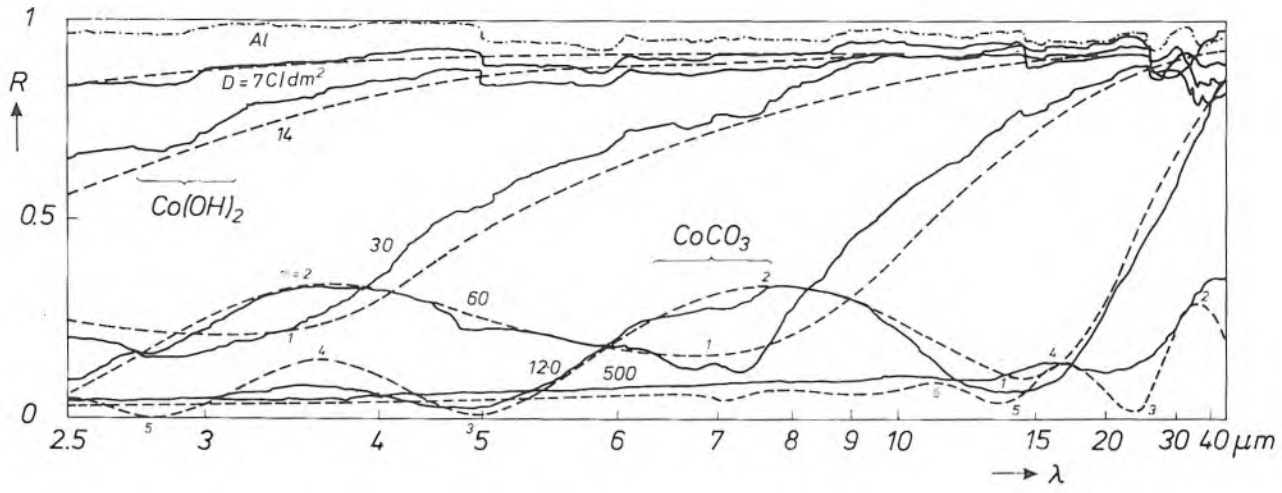


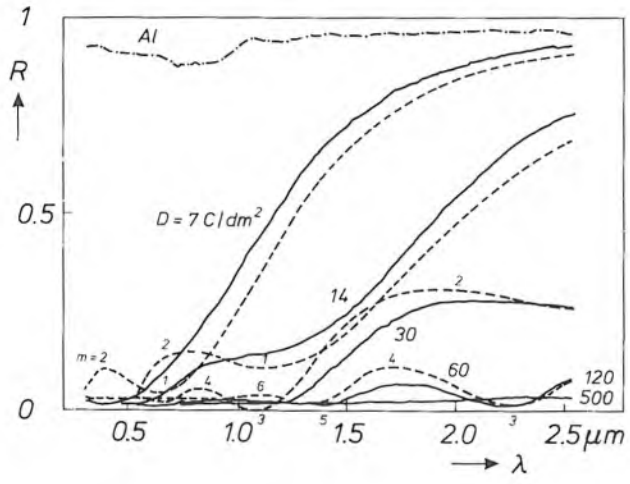


Fig. 2. Measured reflectance $R$ plotted against wavelength $\lambda$ in the infrared (*a*) and the solar wavelength range (*b*), for black-cobalt coatings with different electrolytic thickness $D$. For comparison the reflectance of an aluminium film (Al) is also given. The dashed curves refer to calculations made using wavelength-dependent functions for the refractive index and the absorption index, and assuming a proportional relation between electrolytic and geometrical thickness (500 C/dm² corresponds to 10 μm). The interference maxima and minima of order $m$ are also indicated. On increasing thickness, the reflectance in the near infrared decreases strongly and the interference maxima and minima shift to longer wavelengths.

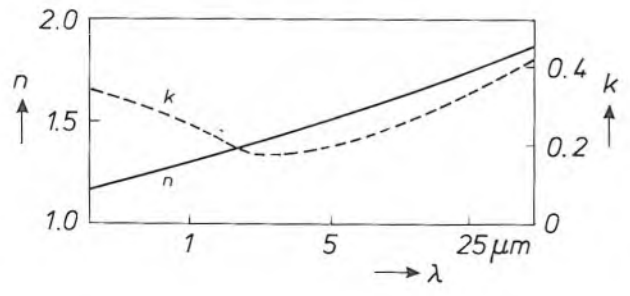


Fig. 3. Refractive index $n$ and absorption index $k$ of black-cobalt coatings as a function of the wavelength $\lambda$. Whereas $n$ increases monotonically with $\lambda$, there is a minimum for $k$ at about 2.5 μm.

Annealing in high vacuum results in two significant changes in the optical properties. After annealing at 350 °C the reflection spectra reveal a significant increase in $k$ for wavelengths between 1 and 15 μm, to an almost constant value of about 0.35. This effect is accompanied by a reduction in thickness of several per cent. A subsequent treatment at 450 °C has no measurable effect on $k$, but a thickness reduction of 25% is now observed which remains constant even after annealing for more than 24 hours.

The effect of annealing on the reflectance in the solar wavelength range is shown in *fig. 5* for a coating of 14 C/dm². The mean value for the solar absorptance still exceeds 90% for a sample annealed at 450 °C. It is important to note that the infrared emissivity of this sample is essentially the same as for a non-annealed sample, since the increase in infrared absorptance is almost exactly compensated by the reduction of 25% in the coating thickness. If the coatings are assumed to be homogeneous with compositions as given in Table I, a decrease in thickness of 33% would be expected. However, the annealing is associated with changes in the porous structure, as has been demonstrated by SEM micrographs.

The considerable influence of the substrate roughness on the morphology of the coatings (fig. 1) has significant consequences for their optical properties. This is illustrated in *fig. 6*, which shows the directional emissivity for coatings of different thicknesses on various substrates. The emission characteristics of the uncoated substrates are found to be very similar, but

[7] See for example R. A. Nyquist and R. O. Kagel, Infrared spectra of inorganic compounds, Academic Press, New York 1971.

[8] H. C. Hottel and A. F. Sarofim, Radiative transfer, McGraw-Hill, New York 1967.

in the case of the coated samples the substrate roughness has a pronounced effect, especially for coatings of 30 C/dm$^2$. In this case the hemispherical emissivity at 133 °C may vary by more than a factor of two. This can be mainly attributed to an enhanced porosity of the coating on rough substrates, which is associated with an increased thickness.

A number of results are summarized in *fig. 7*, where the normal and hemispherical infrared emissivities are given as a function of the electrolytic thickness. Because of the broadband infrared absorption of the black cobalt, the coating thickness is the most important parameter for the emissivity. The same is true for the solar absorptance, which is also shown in fig. 7.

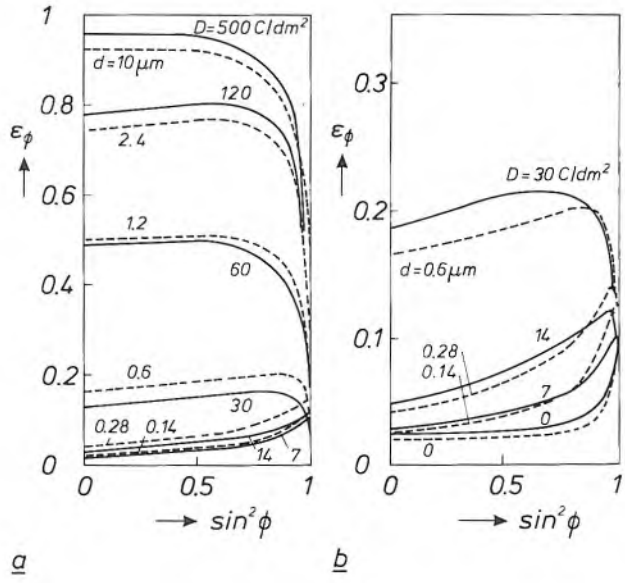


**Fig. 4.** Directional thermal emissivity $\varepsilon_\phi$ at 127 °C as a function of $\sin^2\phi$ for two series of black-cobalt coatings. The continuous curves were obtained from measurements on coatings with different electrolytic thickness $D$. The dashed curves refer to calculations for different values of the geometrical thickness $d$. For coatings of thickness up to 60 C/dm$^2$ the directional emissivity differs increasingly from that of an uncoated copper surface ($D$ = 0 C/dm$^2$). The thicker coatings have an emissivity that is characteristic of a weak absorber.

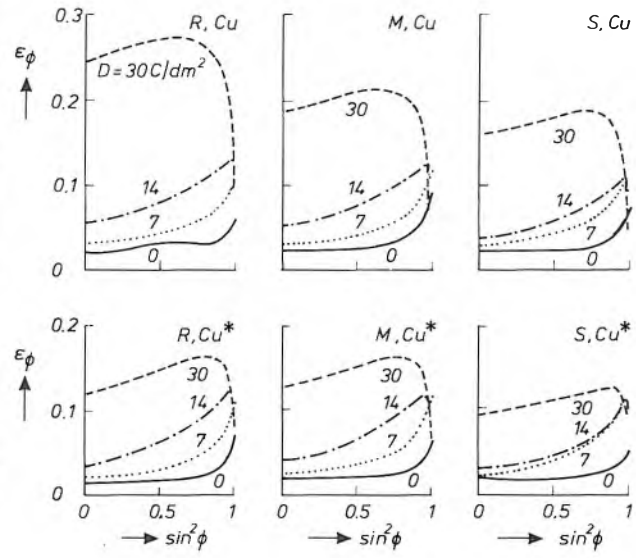


**Fig. 6.** Directional thermal emissivity $\varepsilon_\phi$ at 133 °C plotted against $\sin^2\phi$ for black-cobalt coatings of different electrolytic thickness $D$. The substrates used are rough ($R$), medium ($G$) or smooth ($S$) and they are coated with 1 μm of copper from a cyanide solution (Cu) or 5 μm of bright copper (Cu*). It can be seen that the coating thickness is the most important parameter for the directional emissivity.

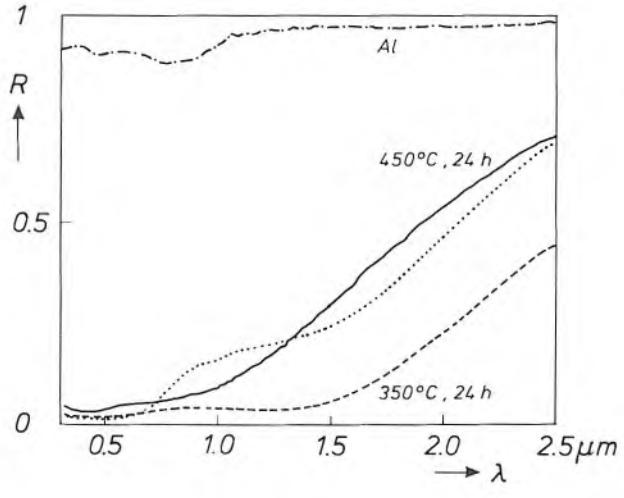


**Fig. 5.** Effect of vacuum annealing on the reflectance in the solar wavelength range, for a cobalt coating of 14 C/dm$^2$ on smooth steel coated with 5 μm of bright copper. Annealing for 24 h at 350 °C (dashed curve) results in an appreciable decrease in reflectance as compared with the non-annealed coating (dotted curve). After annealing for a further 24 h at 450 °C (continuous curve) the original near-infrared reflectance is almost completely restored.

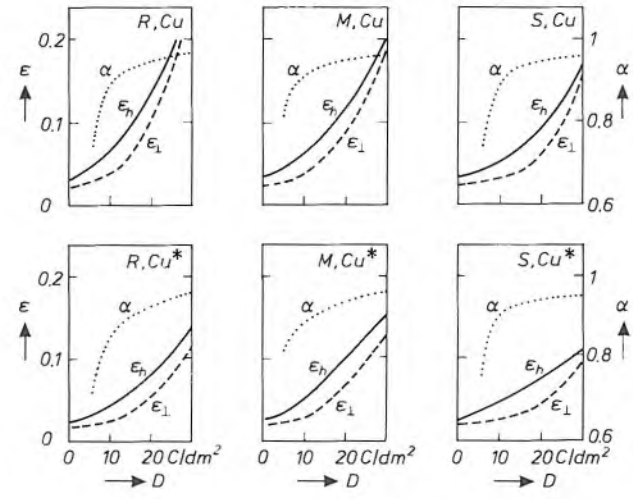


**Fig. 7.** Solar absorptance $\alpha$ (at room temperature) and the thermal emissivities $\varepsilon_\perp$ and $\varepsilon_h$ (both at 133 °C) as a function of the electrolytic thickness $D$ for the samples of fig. 6. The properties of the substrate have a much smaller effect on $\alpha$ than on $\varepsilon_\perp$ and $\varepsilon_h$. The best results are obtained on a smooth substrate with 5 μm of bright copper, giving $\alpha$ = 93% and $\varepsilon_h$ = 5% for a cobalt coating of 14 C/dm$^2$.

However, whereas the emission properties depend significantly on the substrate properties, the solar absorptance is much less affected. The requirements of a high solar absorptance and a low infrared emissivity are best met with a coating thickness of 14 C/dm$^2$ on a smooth steel substrate coated with bright copper. In this case the solar absorptance is as high as 93% and the hemispherical emissivity at 133 °C is as low as 5%.

### Performance in a non-inert atmosphere

A thin black-cobalt coating changes considerably when exposed to air at elevated temperatures. For example, during a one-hour anneal in air at about 250 °C its colour changes from black to a golden or brownish hue, with a marked reduction in the solar absorptance. SEM micrographs show that the coating is still present, and that its morphology is unchanged. The formation of a more transparent coating is due to the oxidation of the cobalt particles to CoO, as has been demonstrated by X-ray diffraction. Further exposure to air leads to the formation of the grey-black oxide $Co_3O_4$ [9] and an oxidation of the reflecting copper film, giving an increased infrared emissivity.

Coatings with reduced solar absorptance were also obtained after annealing under poor vacuum conditions (≈ 1 Pa) at higher temperatures (350 °C) and longer exposure times. The resulting reflectance in the solar wavelength range is shown in *fig. 8* for a coating of 14 C/dm$^2$. For comparison, the spectra before annealing and before coating are also shown. Absorption data for CoO [10] were also used to calculate the spectrum for an oxidized coating. The resulting curve is close to the one measured after annealing, which confirms the above assumptions.

Annealing at 450 °C in a poor vacuum (≈ 1 Pa) may lead to severe degradation of the surface, related to the quality of the copper film. *Fig. 9* shows SEM micrographs of two surfaces with such a degradation. Both contain outgrowths which can be observed at different stages of the growth. X-ray diffraction and X-ray fluorescence analysis indicate that these outgrowths consist of crystalline $\gamma$-$Fe_2O_3$. This oxide has a broadband infrared absorption [7] and the arrangement of the outgrowths also forms a resonance structure for the infrared wavelengths. This degradation can therefore be responsible for values of the emissivity which are between the value for black cobalt and a

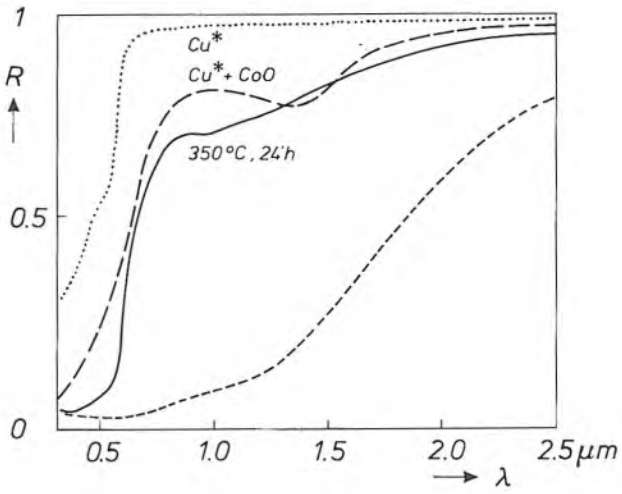


Fig. 8. Effect of annealing for 24 h at 350 °C in poor vacuum (≈ 1 Pa) on the reflectance of a black-cobalt coating of 14 C/dm$^2$ in the solar wavelength range. The dotted curve refers to the bright-copper reflector, the lower dashed curve and the continuous curve to the cobalt coating before and after annealing. The strong increase in reflectance can be simulated fairly well. The upper dashed curve was calculated for 0.26 μm of CoO on bright copper.

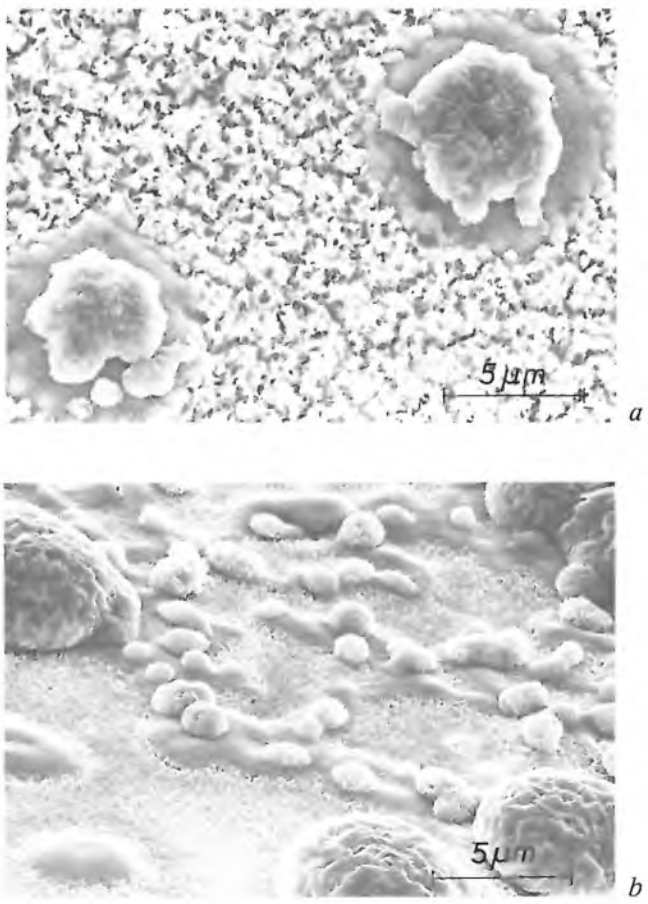


Fig. 9. SEM micrographs of two coatings, showing the effect of annealing for 24 h at 450 °C in poor vacuum, with an insufficient coating of copper on the steel substrate. For a cobalt coating of 60 C/dm$^2$ on 1 μm of cyanidic copper (*a*) large outgrowths are formed. For a coating of 14 C/dm$^2$ on 0.5 μm of cyanidic copper (*b*) many outgrowths of different sizes are observed.

[9] The formation and properties of this oxide have been described by several authors, including:
T. Tanaka, Jap. J. Appl. Phys. **18**, 1043-1047, 1979; and C. Choudhury and H. K. Sehgal, Sol. Energy **28**, 25-31, 1982.

[10] I. G. Austin, B. D. Clay and C. E. Turner, Optical absorption of small polarons in semiconducting NiO and CoO in the near and far infra-red, J. Phys. C **1**, 1418-1434, 1968.

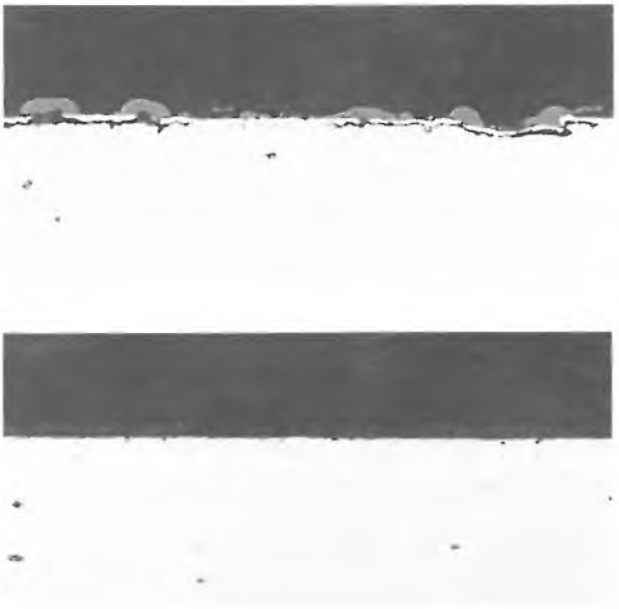

Fig. 10. Micrographs of polished cuts of two coated steel substrates with different copper films, after annealing under the same conditions. The degradation (*a*) found with the sample of fig. 9*b* does not occur when the substrate is coated with 5 μm of bright copper (*b*).

The infrared reflection spectra of some annealed copper films on steel substrates are shown in *fig. 11*. The thinner films exhibit a low reflection in the near infrared and characteristic $Fe_2O_3$ peaks at long wavelengths. The 5-μm film, on the other hand, gives a high infrared reflection which is not very different from that of a reflecting aluminium film.

### Effect on collector performance

Some ten years of experience of the use of black-cobalt coatings in the Philips evacuated collector tubes [2]–[4] has now been accumulated. In recent collector designs the maximum absorber temperature is about 250 °C. Further optimization may however allow increased stagnation temperatures, especially if an optimized coating is used. In such a case, the coating will have to withstand temperatures of up to 350 °C. Our present results indicate that an optimized coating, carefully annealed at 450 °C under inert conditions, has sufficient stability to maintain a high tube efficiency for more than fifteen years.

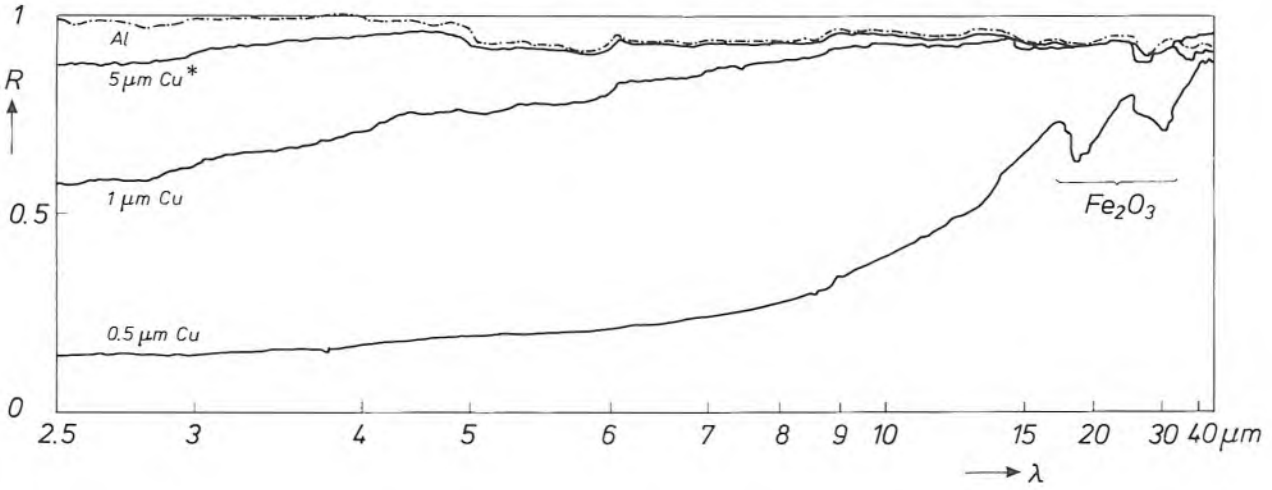


Fig. 11. Infrared reflection spectra of steel substrates coated with various copper films, after annealing for 24 h at 450 °C in poor vacuum. An insufficient coating results in too low an infrared reflectance and vibrational $Fe_2O_3$ peaks due to a partial oxidation of the steel. With 5 μm of bright copper the reflectance is very like that of a reflective aluminium film.

value close to 1, the emissivity of an ideal black-body radiator.

To explain this degradation, it is assumed that the steel of the substrate is attacked by oxygen or $OH^-$ groups via the semipermeable copper film, which is 0.5 or 1 μm thick in the examples of fig. 9. The $Fe_2O_3$ formed by the oxidation is transported to the surface via tunnels in the copper film, as can be seen in the micrograph of *fig. 10a*. Chemical attack by oxygen or water and the resulting degradation can however be avoided by using a 5-μm film of bright copper; see fig. 10*b*.

The most important characteristics for the collector performance — the solar absorptance $\alpha$ and the thermal emissivity $\varepsilon$ — both increase with coating thickness [11]. The thickness dependence of the solar absorptance $\alpha$ and the hemispherical emissivity $\varepsilon_h$ at 127 °C (400 K) for optimized coatings can be expressed as

$$\alpha = 0.975 - 0.815 \exp(-0.22\,D),$$
$$\varepsilon_h = 0.022 + 0.0016\,D + 4.5 \times 10^{-5} D^2,$$

where $D$ is the electrolytic thickness in C/dm$^2$. The increase in the thermal emissivity with temperature for

various thicknesses is illustrated in *fig. 12*. The calculated curves are also shown, made with the assumption that the dielectric properties of the coating are temperature-independent in this range. The emissivity increases linearly with temperature, and the slope $\gamma$ (i.e. the temperature coefficient) increases linearly with the coating thickness:

$$\varepsilon_h(D,T) = \varepsilon_h(D, 400\text{ K}) + \gamma(D) \times (T - 400\text{ K}),$$
$$\gamma(D) = (1.52\,D - 6.65) \times 10^{-5}\text{ K}^{-1},$$

for $D \geqslant 7$ C/dm$^2$. These results can be explained by the shift of the Planckian radiation distribution to shorter wavelengths and the reduction in the near infrared reflectance with increasing thickness (fig. 2).

The results obtained were used for the evaluation of the collector performance. This was done for an improved version of the Philips VTR 361 solar collector tube [4], which has an aluminium reflector. The calculations were based on a validated model for evacuated tubular collectors [5].

The collector efficiency $\eta$ is defined as the power delivered to the heat-transfer fluid (e.g. water or oil) in the collector system divided by the incident radiant power. The useful power delivered to the heat-transfer fluid is equal to the power $Q_a$ absorbed by the plate less the thermal loss $Q_l$, whereas the incident radiation power is given by the solar irradiance $G_T$ (in W/m$^2$) multiplied by the aperture area $A$ (in m$^2$) of the collector, so that:

$$\eta = (Q_a - Q_l)/AG_T.$$

The ratio $Q_a/AG_T$ is referred to as the conversion efficiency $\eta_0$, and $Q_l/A$ is proportional to the overall heat-transfer coefficient $U_l$ (in W/m$^2$K) and to the average difference $\Delta T$ between the fluid temperature in the upper heat pipe of the collector [4] and the ambient temperature. The efficiency can therefore be expressed as

$$\eta = \eta_0 - F'U_l\,\Delta T/G_T,$$

where $F'$ ($\leqslant 1$) is a dimensionless factor to take account of the heat resistance between absorber and heat-transfer fluid.

In *fig. 13* the calculated values of the conversion efficiency $\eta_0$ and the heat-loss coefficient $F'U_l$ are shown as a function of the coating thickness for various values of $\Delta T$. The collector efficiency for any operating conditions can be obtained from these curves and the above equation.

The heat-loss coefficient $F'U_l$ is found to increase considerably with increasing coating thickness. Its temperature dependence is determined both by the $T^4$ radiation law and by the temperature dependence of the emissivity itself. For an adequate conversion efficiency $\eta_0$, a minimum electrolytic thickness of about 8 C/dm$^2$ is required. It should be noted that a performance with $\eta_0 \geqslant 0.70$ and $F'U_l < 1$ W/m$^2$K is possible for low-temperature applications ($\Delta T \approx 50$ K). In high-temperature applications ($\Delta T \approx 200$ K) $\eta_0$ can

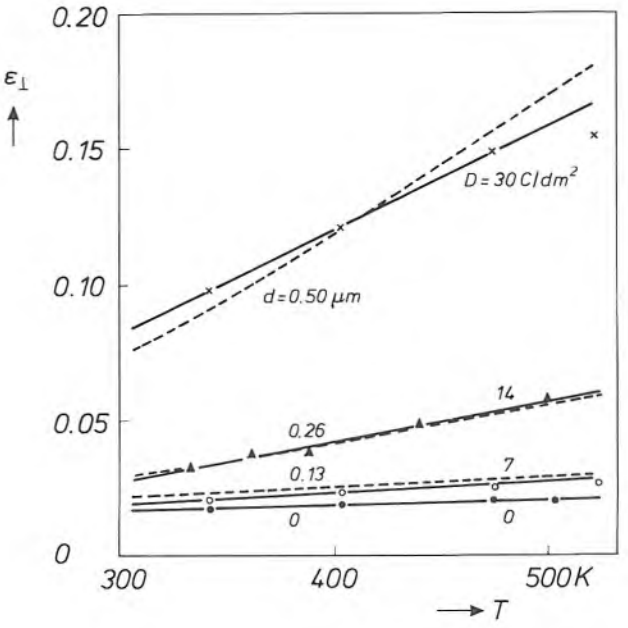


Fig. 12. Temperature dependence of the thermal emissivity $\varepsilon_\perp$ for black-cobalt coatings with different electrolytic thicknesses $D$ (continuous curves) and calculated for different geometrical thicknesses $d$ (dashed curves). It is seen that $\varepsilon_\perp$ depends linearly on the absolute temperature $T$, and that the slope increases for thicker coatings.

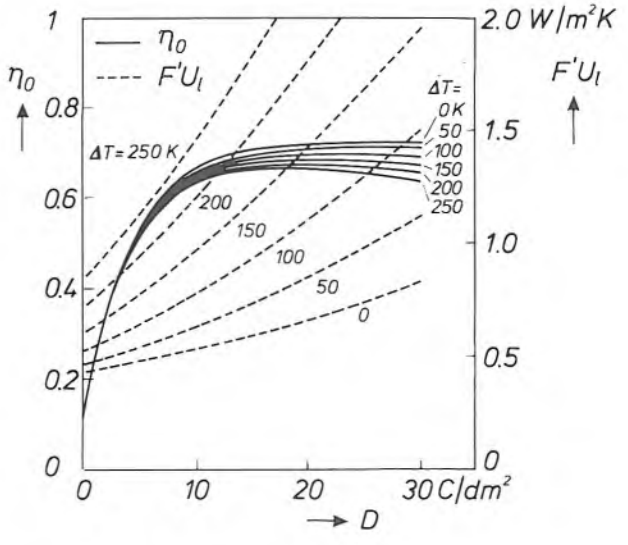


Fig. 13. Calculated performance of a solar collector (VTR 361 tubes with heat pipe and an aluminium reflector). The conversion efficiency $\eta_0$ and the heat-loss coefficient $F'U_l$ (see text) are plotted against the electrolytic thickness $D$ of optimized coatings for different values of the average difference $\Delta T$ between the heat-transfer fluid temperature in the upper heat pipe and the ambient temperature.

[11] General information on the use of solar energy can be found in: J. A. Duffie and W. A. Beckman, Solar engineering of thermal processes, Wiley, New York 1980.

still be as high as 0.60 or more, with $F'U_l \approx 1.20$ W/m$^2$K.

These performance results can be converted into annual efficiencies by a simple method [6]. The values were calculated for climatic conditions characteristic of two European climatic zones; see *fig. 14*. Obviously, different coating thicknesses should be used: 15 C/dm$^2$ for low-temperature applications and 10 C/dm$^2$ for high-temperature applications. In the latter case annual efficiencies of more than 20% are possible in a sunny climate with permanent operation at $\Delta T = 200$ K.

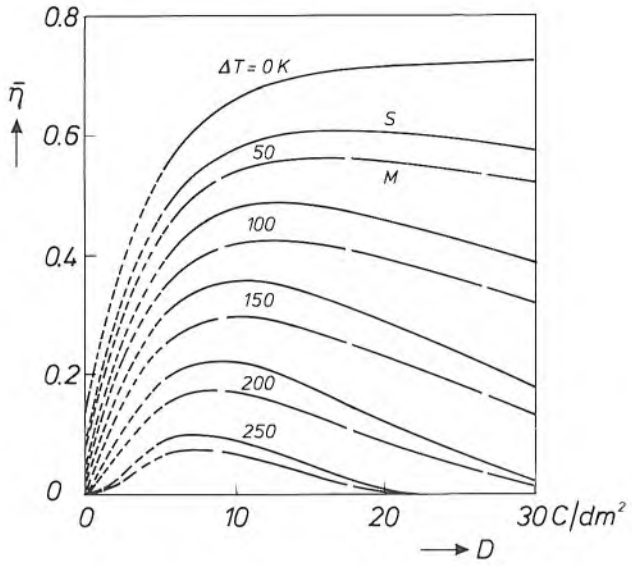


**Fig. 14.** Annual efficiency $\bar{\eta}$ of a Philips evacuated tubular collector as a function of the electrolytic coating thickness $D$, calculated for two different European climatic zones ($S$ Southern Europe, $M$ Central Europe) and for different values of the mean operating temperature difference $\Delta T$. The optimum coating thickness can be derived for a given application with a known value of $\Delta T$.

Valuable contributions to the work described here were made by our colleagues at the laboratories in Aachen and the Philips Plastics and Metalware Factories in Eindhoven.

**Summary.** In the evacuated receiver tubes of a solar collector an absorber plate with a spectrally selective black-cobalt coating is used for reducing the thermal radiation losses. The influence of the substrate roughness and annealing conditions on the structure and composition of the coatings greatly affects their high-temperature stability and thermo-optical properties. The most suitable coatings for high-temperature application are obtained on smooth substrates after vacuum-annealing at about 450 °C. The optimum electrolytic coating thickness for the required optical selectivity is generally less than 30 C/dm$^2$, depending on the intended temperature range in the collector. The stability of optimized coatings seems to be sufficient for use in solar collectors designed for high-temperature applications (150-250 °C).

# Research on television glass

D. M. Krol and R. K. Janssen

*The mass production of glass has long been a stronghold of empiricism, but science is now an increasing presence. Much of the initiative for this comes from the Central Glass Laboratory, set up in 1957, and from Philips Research Laboratories. Following on from an earlier study at Philips Research Laboratories on the 'fining' of glass, described previously in this journal, attempts have been made to obtain a scientifically based understanding of a wider field of the glass-formation processes, including both melting and fining. The glass compositions used in these studies were made as close as possible to those used in practice.*

## Introduction

The average home in the western world contains a television set. The glass for the picture tube is as likely as not made in a Philips pressed-glass works. Against this background and the fact that glass also forms an indispensable component for many other Philips products, it is not surprising that studies on glass are regularly reported in this journal [1].

The glass for picture tubes is generally formed in a continuous process by subjecting a mix of raw materials to a treatment in which the temperature varies with time in a special predetermined pattern [2]. The mix for this application consists of alkali metals and alkaline-earth metals combined as oxides and carbonates, $SiO_2$, $Al_2O_3$ as feldspar and a number of special additives, and cullet. The temperature-time treatment takes place in furnaces constructed from separate, but closely fitting, blocks of refractory material. A diagram of a widely used version of such a furnace, which can contain 300 tonnes of glass, is shown in *fig. 1*; *fig. 2* is a view of the interior of such a furnace.

The mix is delivered via the 'batch hopper' *B* to the 'melting end' *M*. This is where the glass-formation reactions take place. The molten glass produced flows through the 'working end' *W* via feeders *F* to the glass-processing machines. After the glass has been formed in the 'melt' phase at about 1350 °C and has become completely fluid, the melt initially contains large quantities of gas bubbles; at this stage the composition of the melt is still highly inhomogeneous in other

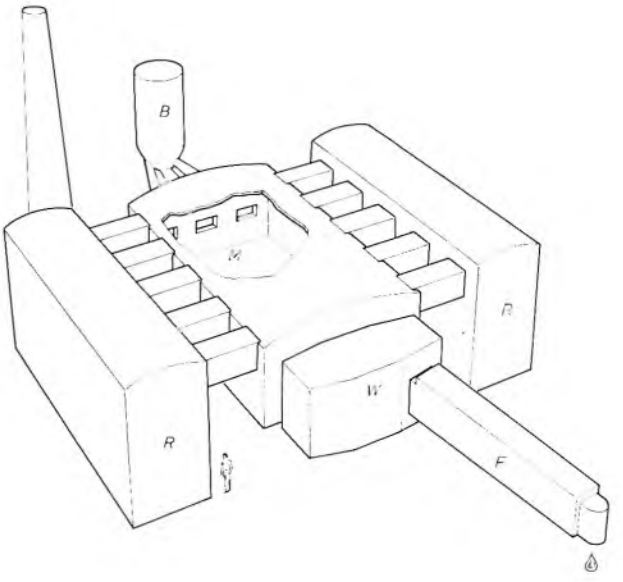


**Fig. 1.** Diagram of furnace for the production of glass for television picture-tube screens. *B* batch hopper. *M* 'melting end'. *W* 'working end'. *F* feeder. The air above the glass melt is heated by burners (not shown). The temperature is held at about 1350 °C in the melting end, and allowed to fall to about 1000 °C for shaping. The way in which the temperature is allowed to vary between these two final values has a considerable effect on the quality of the glass produced. The regenerators *R* preheat the air with heat derived in part from the flue gases. A furnace such as this can contain 300 tonnes of glass, with a production of 90 tonnes a day.

*Dr D. M. Krol, formerly with Philips Research Laboratories, Eindhoven, is now with AT&T Bell Labs, Murray Hill, New Jersey, U.S.A.; Ing. R. K. Janssen is with Philips Research Laboratories, Eindhoven.*

[1] See for example the issue devoted entirely to glass: Philips Tech. Rev. **22**, 281-341, 1960/61, and the recent article: A. Kats, Glass — outline of a development, Philips Tech. Rev. **42**, 316-324, 1986.

[2] See for example: G. E. Rindone, Glass Ind. **38**, 489-528, 1957; J. Stanek, J. Non-Cryst. Solids **26**, 158-178, 1977.

**Fig. 2.** Looking into a glass furnace at the Philips glassworks in Aachen, West Germany. The mix enters the furnace through the three openings on the left of the furnace, to form the 'sandbanks' further along in the 'river' of molten glass. The furnace is 7 m wide and 15 m long, and contains a glass melt about 1 m deep. Above is one of the burners that melt the mix at a temperature of about 1350 °C.

respects. As the melt continues to flow through the furnace, the bubbles disappear in a 'fining' process, and the melt becomes more homogeneous. Finally, the temperature decreases slowly to about 1000 °C, and the shaping processes can be started. The glass remains in the furnace for about 50 hours on average.

Among the special additives included with the raw materials, the fining agents are particularly important; they are often antimony compounds in combination with $NaNO_3$. The cullet, which always accounts for a fairly large proportion of the ingredients, is added to reduce the process temperature. In an earlier study at Philips Research Laboratories it was shown that Raman spectrometry can be extremely useful for studying the fining of glass [3], largely because the presence of both crystalline and liquid compounds can be established with this method. This study was performed on a glass system obtained by melting 70 mol% of $SiO_2$ and 30 mol% of $K_2CO_3$; only two or three different compounds are produced in the glass formation in this system.

In this article we describe new investigations at Philips Research Laboratories on the formation of glass, with particular relevance to glass for colour television screens. Since we wanted to start with a more realistic glass composition than in the previous study, which implied that the experiments would be more complex, we split the investigation into two parts: we investigated the melting stage and the fining stage separately. For the investigations on the melting stage we used a glass composition that is indeed closer to the actual composition of the television glass: $15Na_2CO_3$-$10BaCO_3$-$75SiO_2$, but is certainly not the same as the composition used in practice (see page 257). In the composition we used the amount of Na corresponds to that of the sum of all the alkali metals, the amount of Ba to that of the sum of all the alkaline-earth metals and the amount of $SiO_2$ to that of all the $SiO_2$ + $Al_2O_3$ in the actual composition.

The only other constituent of the mix that we included in the study was the $NaNO_3$. We did not include the fining agent antimony, assuming that its action would only be observable in the fining stage. With these restrictions, we endeavoured to follow all the conversions by using laser-Raman spectrometry.

In the investigations on the fining stage we chose a type of glass corresponding so closely to the glass used in practice that it was no longer practical to use Raman spectrometry, because of the complexity of the spectra. In this study we have confined ourselves to the effect of the fining agent, antimony, with special attention to the effect of the $Sb^{3+}/Sb^{5+}$ ratio, which we considered relevant. We determined this ratio by potentiometric titration and emission spectrometry.

## Investigation of the melting stage

### *Measurements on samples consisting entirely of raw material*

In our first series of investigations we wanted to obtain a picture of the variety of phases, both crystalline and amorphous, that can arise in a relatively 'realistic'

glass composition during the melting as a function of temperature and time. To start with we therefore subjected samples consisting of the raw materials $Na_2CO_3$, $BaCO_3$ and $\alpha$-quartz (i.e. without special additives) to temperatures between 700 and 1400 °C for periods of 5 minutes to 16 hours, and then quenched them to room temperature. *Fig. 3* gives a number of Raman spectra for the samples treated in this way [4]. The sharp peaks correspond to crystalline phases, the broad bands to amorphous phases or — at higher temperatures — to liquid phases. The identification of

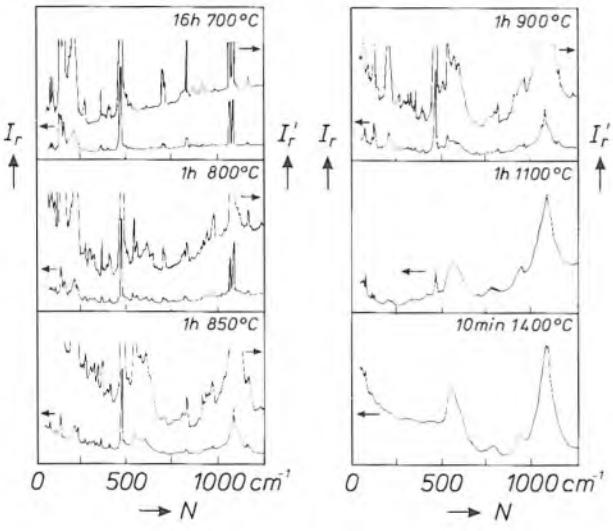


Fig. 3. Raman spectra of mixes consisting of 15 mol% of $NaCO_3$, 10 mol% of $BaCO_3$ and 75 mol% of $SiO_2$ that have been heated for different times and at different temperatures (shown top right) and then quenched to room temperature. The intensity $I_r$ is shown as a function of the wave number $N$ in arbitrary units; at the four lowest temperatures it is also shown with a unit five times as large ($I_r'$).

these peaks and bands was done largely with the aid of compounds we made specially for the purpose (*Table I*). *Table II* indicates the temperature range in which the various compounds can occur.

These Tables lead us to the following conclusions:

- Up to 800 to 900 °C the spectra chiefly originate from crystalline phases — produced in solid-state reactions. A significant amount of the raw material $SiO_2$ (about half) has already been used up in solid-state reactions at 800 °C.
- Above 1000 °C all the spectra are due to liquid phases, with the exception of $\alpha$-quartz, which has been dispersed in the melt in crystalline form.
- As the temperature increases there is a 'condensation', in which silicates with an increasing content of silicon are formed. At 700-800 °C the silicates are mainly ortho- and pyrosilicates, at 850 and 900 °C they are mainly meta- and disilicates.

*The influence of $NaNO_3$*

From the results of a Raman-spectrometric investigation in which $NaNO_3$ was also involved [5] (*fig. 4a* and *b*) it was found that the addition of $NaNO_3$ to the raw materials mentioned above led to a *more rapid* formation of the *same* reaction products in the temperature range around 700 °C, where the solid-state reactions are dominant; when the samples are heated at 1000 °C, with and without $NaNO_3$, the spectra are identical.

We have been able to confirm the first result by a study in which the effect of heating for an hour at 700 °C with $NaNO_3$ was compared with the effect of heating for 16 hours at 700 °C without $NaNO_3$ (*fig. 5*). In spite of the much longer heating time fewer reaction products were formed in the sample without $NaNO_3$.

Since the $NaNO_3$ is only found to have an effect in the temperature range where solid-state reactions are dominant, its action could possibly come about because it assists the formation of a liquid phase below 700 °C. In this liquid phase $Na_2CO_3$ and $BaCO_3$ in the dissolved state would be able to react more quickly with $\alpha$-quartz than they would in the solid state.

Since no data are available about the phase diagram of the system $Na_2CO_3$-$NaNO_3$-$BaCO_3$, we have tested this assumption about the action of $NaNO_3$ by heating a mix of these substances, in the correct proportions, to 700 °C. This mix did indeed go into the liquid phase at this temperature.

## Investigation of the fining stage

In studying the very complex fining action the following three points should be borne in mind:

a) The glass melt contains impurities in the form of bubbles; in addition to nitrogen and water from the atmosphere the melt always contains large quantities of the $CO_2$ generated in the solid-state reactions. Since the purpose of the fining is to remove all the bubbles from the glass, it is important that the solid-state reactions should be fully completed before the fining mechanism comes into action.

b) The fining mechanism is brought into action by the conversion of $Sb^{5+}$ from the added fining agent into $Sb^{3+}$ with the formation of oxygen, which rises to the surface in the form of bubbles. This oxygen formation at the same time aids the growth of the other bubbles present in the glass, which also rise to the surface.

[3] See for example H. Verweij, Philips Tech. Rev. **40**, 310-315, 1982.

[4] A more detailed account of this investigation is given in: D. M. Krol and R. K. Janssen, J. Physique **43** (Colloque C9), C9/347-C9/350, 1982.

[5] A more detailed account of this investigation is given in: D. M. Krol and R. K. Janssen, Glastech. Ber. **56K**, 1-6, 1983.

**Table I.** Position and intensity of the Raman lines of a number of crystalline compounds that we prepared, for the identification of the Raman spectra we measured. The position is indicated by the wave number in $cm^{-1}$. Lines of intensity greater than 90% of the intensity of the strongest line are shown in red, intensity values between 70% and 90%, 30% and 70%, 10% and 30%, 5% and 10%, and between 0 and 5% are indicated by the letters S, M, W, VW and F, respectively. A dash indicates that the compound could not be obtained in a sufficiently pure form to give a good Raman spectrum.

| Compound | | Position and intensity of Raman line | | | | | | |
|---|---|---|---|---|---|---|---|---|
| Raw materials | $Na_2CO_3$ | 188W | 700VW | 1080 | 1432F | 1770F | | |
| | $BaCO_3$ | 139M | 154M | 224VW | 691W | 1060 | 1423F | 1508F |
| | | 1770F | | | | | | |
| | $\alpha$-quartz | 128M | 206W | 264VW | 356VW | 395F | 402F | 465 |
| | | 698F | 795F | 807F | 1067F | 1083F | 1162F | |
| Ortho-silicates | $Na_4SiO_4$ | — | | | | | | |
| | $Ba_2SiO_4$ | 370VW | 498W | 522VW | 823 | 860W | 888VW | 914W |
| Pyro-silicates | $Na_6Si_2O_7$ | 535VW | 597W | 842 | 881VW | 919M | 1028M | |
| | $Na_2Ba_2Si_2O_7$ | 300VW | 320W | 363W | 376W | 507VW | 614VW | 820 |
| | | 883VW | 912M | 946VW | 993VW | 1080W | | |
| Meta-silicates | $Na_2SiO_3$ | 400W | 586W | 971 | 1020VW | | | |
| | $BaSiO_3$ | 312M | 396W | 407W | 535VW | 548VW | 600S | 928VW |
| | | 965 | 1062W | | | | | |
| | $Na_2BaSi_2O_6$ | 266VW | 290W | 366VW | 391W | 479VW | 520VW | 554VW |
| | | 631S | 891VW | 897W | 958 | 1000M | 1056W | |
| | $Ba_2Si_3O_8$ | — | | | | | | |
| | $Ba_5Si_8O_{21}$ | 288W | 312W | 502W | 536M | 550M | 614W | 926W |
| | | 1067 | | | | | | |
| | $Ba_3Si_5O_{13}$ | — | | | | | | |
| Di-silicates | $\alpha$-$Na_2Si_2O_5$ | 312VW | 391W | 502M | 968VW | 1016W | 1061M | 1076 |
| | $\beta$-$BaSi_2O_5$ | 269VW | 292VW | 316W | 333W | 476VW | 535M | 1078 |
| | $Na_2Ba_4Si_{10}O_{25}$ | 273W | 298W | 321W | 348W | 463W | 508M | 573M |
| | | 1081 | | | | | | |
| Tri-silicates | $Na_6Si_8O_{19}$ | 357W | 413W | 494 | 540M | 792VW | 1061? | 1130W |
| | $Na_2Si_3O_7$ | — | | | | | | |

**Table II.** The distribution of the phases shown in the Raman-spectrometric investigation of the system $15Na_2O$-$10BaCO_3$-$75SiO_2$ in the temperature range from 700 to 1400 °C.

| | $T$ (°C) | 700 | | 800 | | 850 | 900 | | 1000 | | | 1100 | | | 1200 | | 1400 | |
|---|---|---|---|---|---|---|---|---|---|---|---|---|---|---|---|---|---|---|
| | $t$ (h) | 1 | 16 | 1 | 16 | 1 | 1 | 16 | $\frac{1}{4}$ | 1 | 16 | $\frac{1}{4}$ | 1 | 16 | $\frac{1}{4}$ | 1 | $\frac{1}{6}$ | $\frac{1}{4}$ |
| Ortho-silicates | $Na_4SiO_4$ | | | | | | | | | | | | | | | | | |
| | $Ba_2SiO_4$ | (x) | x | x | x | | | | | | | | | | | | | |
| Pyro-silicates | $Na_6Si_2O_7$ | | | | | | | | | | | | | | | | | |
| | $Na_2Ba_2Si_2O_7$ | | x | x | x | x | x | x | x | | | | | | | | | |
| Meta-silicates | $Na_2SiO_3$ | | (x) | | | | | | | | | | | | | | | |
| | $BaSiO_3$ | | | x | x | x | x | x | x | | | | | | | | | |
| | $Na_2BaSiO_6$ | | | x | x | | | | | | | | | | | | | |
| | $Ba_2Si_3O_8$ | | | | | | | | | | | | | | | | | |
| | $Ba_5Si_8O_{21}$ | | | x | x | x | | | | | | | | | | | | |
| | $Ba_3Si_5O_{13}$ | | | | | | | | | | | | | | | | | |
| Di-silicates | $\alpha$-$Na_2Si_2O_5$ | | | | | | | | | | | | | | | | | |
| | $\beta$-$BaSi_2O_5$ | | | | | x | x | x | | x | | | | | | | | |
| | $Na_2Ba_4Si_{10}O_{25}$ | | | | | x | x | x | | | | | | | | | | |
| Tri-silicates | $Na_6Si_8O_{19}$ | | | | | | | | | | | | | | | | | |
| | $Na_2Si_3O_7$ | | | | | | | | | | | | | | | | | |
| | $\alpha$-quartz | x | x | x | x | x | x | x | x | x | x | x | x | | x | | | |
| | $\alpha$-crystobalite | | | | | | | | | (x) | x | x | x | | x | | | |
| Liquid di- or tri-silicates | | | | | | | | | x | x | x | x | x | x | x | x | x | x |

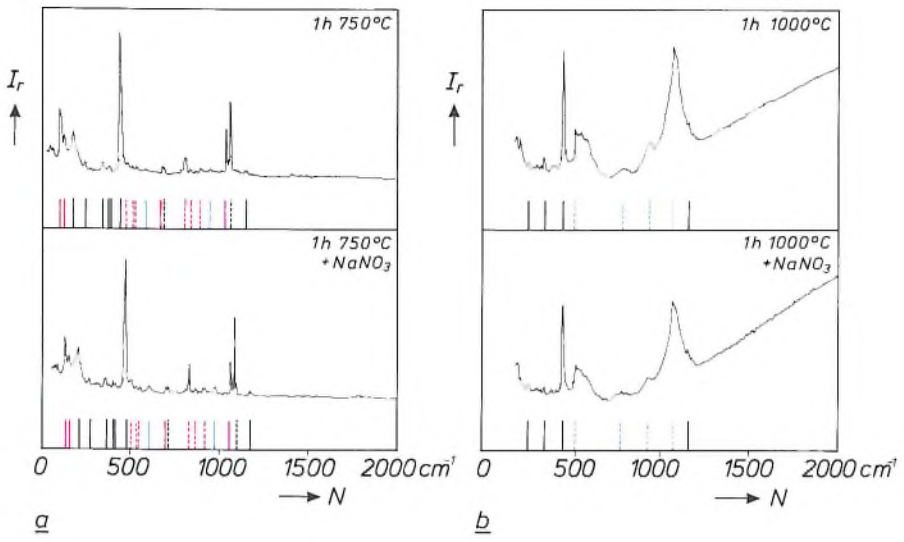


**Fig. 4.** As fig. 3, but here the spectra shown below originate from samples with added $NaNO_3$. The peaks here have been identified as originating from $\alpha$-quartz (short black vertical line), $Na_2CO_3$ (black dashed line); $BaCO_3$ (red line), $Ba_2SiO_4$ + $Na_2Si_2O_7$ (red dotted line), $BaSiO_3$ (blue line) and liquid disilicate (blue dashed line).

c) At the end of the fining stage the glass melt only contains small bubbles, which mainly consist of oxygen. If the temperature decreases, the oxygen in these bubbles goes into solution again in the melt, so that the bubbles are 'reabsorbed'.

In our study of the fining stage [6] we have worked with a glass composition that was very close to the composition used in practice: the raw-materials mix that we prepared consisted of $SiO_2$, $Al_2O_3$, $K_2CO_3$, $Na_2CO_3$, MgO, $CaCO_3$, $SrCO_3$, $BaCO_3$ in mole percentages of 72, 2.2, 4.9, 10.15, 2.15, 2.1, 0.15 and 5.6 respectively. Although earlier investigations included $Sb_2O_3$, we did not use this now little-used material. Instead we used 0.1 mol% of $NaSbO_3.H_2O$, which is also used in practice. We also added 0.65 mol% of $NaNO_3$.

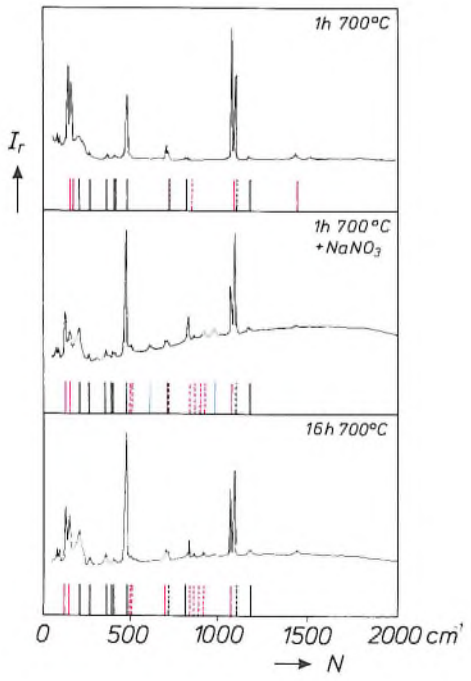


**Fig. 5.** As in fig. 4, but here the sample without $NaNO_3$ has been heated again for a further 16 hours (below). Heating for one hour with $NaNO_3$ (centre) is always found to produce more reaction products than heating for 16 hours without $NaNO_3$.

These samples were heated for 30 minutes, 10, 20 or 200 hours at various temperatures and then quenched to room temperature. With this realistic glass composition, as we mentioned earlier, Raman spectrometry is no longer the preferable method for studying the reactions. We confined ourselves to following the change in the equilibrium of the redox couple $Sb^{3+}/Sb^{5+}$, by determining the quantity of $Sb^{3+}$ ions by potentiometric titration and the total amount of Sb ($Sb_T$) by emission spectrometry.

Some results are given in *Table III*. On increasing the temperature, the oxidation-reduction equilibrium evidently shifts towards $Sb^{3+}$, which leads to the desired formation of oxygen. This seemed to indicate that at temperatures above 1000 °C equilibrium would be reached after only 10 hours. However, further investigation showed that this conclusion was not justified. It was found, for example, that on heating at 1200 °C for a much longer period, 200 hours, the equilibrium continued to shift, with the $Sb^{3+}/Sb^{5+}$ ratio changing from 0.58 (after heating for 20 hours) to 0.67 (see also Table IV).

[6] A more detailed account of this investigation is given in: D. M. Krol and P. J. Rommers, Glass Technol. **25**, 115-118, 1984.

**Table III.** The ratio $Sb^{3+}/Sb_T$ for 'raw-materials samples' as a function of the temperature $T$ to which they have been subjected for 0.5, 10 or 20 hours.

| $T$ (°C) | Time | | |
|---|---|---|---|
| | 0.5 h | 10 h | 20 h |
| 900 | 0.011 ± 0.006 | 0.018 ± 0.009 | 0.030 ± 0.004 |
| 1000 | 0.029 ± 0.015 | 0.100 ± 0.008 | 0.107 ± 0.009 |
| 1100 | 0.14 ± 0.02 | 0.28 ± 0.02 | 0.32 ± 0.02 |
| 1200 | 0.45 ± 0.03 | 0.60 ± 0.04 | 0.58 ± 0.04 |
| 1300 | 0.62 ± 0.05 | 0.79 ± 0.05 | 0.76 ± 0.05 |
| 1400 | 0.75 ± 0.05 | 0.89 ± 0.06 | 0.87 ± 0.06 |
| 1500 | 0.84 ± 0.05 | 1.00 ± 0.07 | 0.93 ± 0.06 |

**Table IV.** The ratio $Sb^{3+}/Sb_T$ for three types of sample that we used; temperature and time for the treatment are given in the Table.

| Types of sample | Temperature | | |
|---|---|---|---|
| | 1000 °C | 1200 °C | 1400 °C |
| Raw materials | | 0.67 (200 h) 0.58 (20 h) | |
| Cullet | | 0.95 (200 h) 0.94 (20 h) | |
| Powdered cullet 4 × 20 h | 0.76 | 0.69 | 0.95 |
| Powdered cullet 5 × 20 h | 0.67 | 0.69 | 0.95 |

Our explanation for this is that the oxidation/reduction ratio $Sb^{3+}/Sb^{5+}$ is determined by two processes:

$$Sb^{5+}\,(\text{glass}) + O^{2-}\,(\text{glass}) \underset{\rightarrow}{\overset{v_1}{\leftarrow}} \tfrac{1}{2}O_2\,(\text{glass}) + Sb^{3+}. \quad (1)$$

$O_2$ (bubbles) ⇄ ($v_1$) ; $O_2$ (glass) ⇄ ($v_2$) $O_2$ (atmosphere)

First of all an equilibrium with the oxygen in the bubbles becomes established at a relatively high rate $v_1$ and an equilibrium with the oxygen in the furnace atmosphere only becomes established later, at a much slower rate $v_2$.

Indications that this hypothesis is correct have also been found in another part of the investigation, where we were particularly interested in studying the effect of the addition of cullet.

We made 'cullet samples' from glass that had been obtained by melting the raw materials described earlier at 1500 °C. The standard procedure was then followed with these 'ordinary cullet samples': heating to temperatures between 900 and 1500 °C and quenching. With the 'powdered cullet samples' this procedure was modified by repeating the heating and cooling in periods of 20 hours, pulverizing the sample again after each cooling.

For the powdered cullet samples we were able to establish that at temperatures of 1200 °C and above there was no further change in the $Sb^{3+}/Sb_T$ content, so that it may be assumed that an equilibrium with the oxygen in the atmosphere is attained at these temperatures after this treatment (*Table IV*). The value of $Sb^{3+}/Sb_T$ found at 1200 °C is then indeed found to be just as high as the value measured for the 'raw-materials sample' at the same temperature after the lengthy treatment for 200 hours.

The values of $Sb^{3+}/Sb_T$ that are found as a function of temperature and time for an 'ordinary cullet sample' are however very different (*fig. 6* and Table IV). In this case the $Sb^{3+}/Sb_T$ content at each temperature has a value in the region of 0.95, i.e. the sample maintains the equilibrium value that it acquired in the initial melt at 1500 °C.

In our view the explanation for this difference is that the oxygen that is necessary for the reoxidation of $Sb^{3+}$ to $Sb^{5+}$ in the non-powdered — massive — cullet sample has to travel a much longer diffusion path than it does in the powdered sample. This seems reasonable because even after 200 hours the diffusion length of $O_2$ at 1200 °C is only $4.4 \times 10^{-2}$ cm, and thus negligibly small compared with the dimensions of the sample. In the powdered cullet sample the oxygen that will diffuse into the interior is present around each separate grain.

This result explains the well-known practical result that the fining agent does not work properly if too much cullet is added to the mix.

Similarly, in the raw-materials sample, if it was only the oxygen from the surrounding atmosphere that was

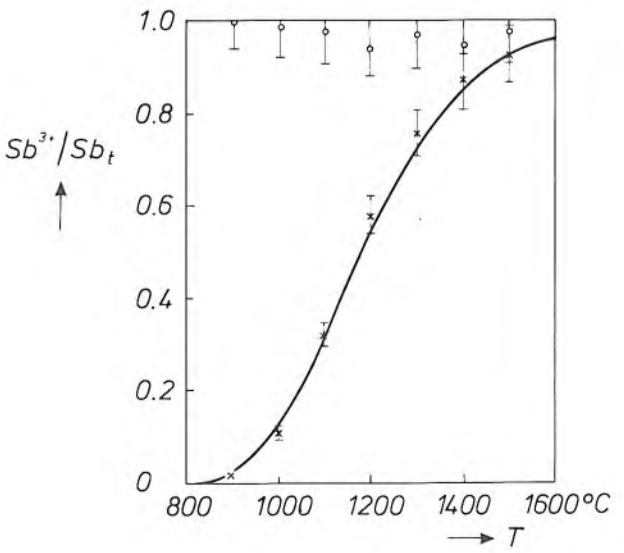


**Fig. 6.** The ratio $Sb^{3+}/Sb_T$ for 'raw-materials samples' (crosses) and 'powdered cullet samples' as a function of the temperature to which the samples have been subjected for 20 hours.

significant, then there would be no reason for expecting that the effect of temperature would result in a noticeable shift of the $Sb^{3+}/Sb^{5+}$ couple, since this shift would be determined by the very slow oxygen-diffusion process. In the raw-materials sample, however, as we have seen, there is the possibility of oxygen occurring in the form of bubbles in the melt, with a partial oxygen pressure of 1 bar. This is a higher oxygen pressure than is reached in the equilibrium state of the powdered cullet sample (0.2 bar). This means that in the raw-materials sample the $Sb^{3+}/Sb_T$ ratio will be lower than in the powdered cullet (corresponding to a high $p_{O_2}$ (glass)) for relatively short melting times (20 hours). From Table IV and fig. 6 we have been able to show that the ratio $Sb^{3+}/Sb^{5+}$ at 1200 °C (after 20 hours) is equal to 1.4 ± 0.2 for a raw-materials sample. For a powdered cullet sample this value is 2.2 ± 0.6.

If in the equilibrium expression

$$K' = \frac{[Sb^{3+}](p_{O_2})^{\frac{1}{2}}}{[Sb^{5+}]},$$

we use the value $p_{O_2} = 0.2$ for the powdered cullet sample, then with the $Sb^{3+}/Sb^{5+}$-values given above for the raw-materials sample we find a $p_{O_2}$-value of 0.5 bar. In view of the experimental uncertainties in the starting points for the calculation, this value agrees reasonably well with the value of 1 bar assumed earlier.

*The influence of $NaNO_3$*

Finally, we shall say a few words about the influence of $NaNO_3$, which, as our results also indicate, becomes evident at the fining stage.

At a temperature of about 550 °C the $NaNO_3$ decomposes accompanied by the formation of oxygen. This means that the oxygen concentration (or more accurately, the oxygen activity) in the glass melt will be increased, and this will happen before it does so under the influence of the equilibrium shift of the redox couple $Sb^{3+}/Sb^{5+}$. It will therefore also increase the temperature at which this shift commences (*fig. 7*). In principle, such an increase in the temperature has the beneficial effect that the formation of oxygen can be 'put off' until the formation of $CO_2$ has been fully completed.

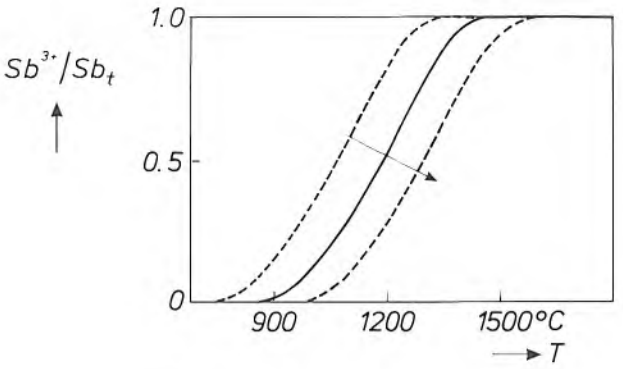


Fig. 7. The ratio $Sb^{3+}/Sb_T$ for raw-materials samples as a function of the temperature to which the samples have been subjected for 20 hours, at varying values of the initial oxygen activity (increasing in the direction of the arrow).

An increase in the initial oxygen concentration by the decomposition of $NaNO_3$ has the additional advantage that less oxygen has to be produced for the melt to be saturated. In this way, therefore, the $NaNO_3$ contributes to the formation, growth and ascent to the surface of the oxygen bubbles and consequently to the removal of the bubbles of $CO_2$, $N_2$, etc.

It is very significant that these are the particular bubbles that are removed, because they are not reabsorbed when the temperature is reduced. And it can be seen from the reaction equation (1) why the remaining oxygen bubbles are indeed absorbed in this case.

Our relatively simple equation therefore helps to explain the empirically well-known beneficial action of the combination of $NaNO_3$ and Sb on the formation of bubble-free glass.

**Summary.** The chemical conversions in the melting stage of glass of the composition $15Na_2CO_3$-$10BaCO_3$-$75SiO_2$ have been investigated with the aid of laser-Raman spectrometry. Below 1000 °C a number of different crystalline compounds are formed, whose silicon content increases with increasing temperature. Between 1000 and 1400 °C the melt consists of liquid disilicates or trisilicates, containing dispersed crystalline α-quartz. The oxidation/reduction equilibrium of the fining agent antimony in glass whose composition closely corresponds to that of television glass has been studied by potentiometric titration and emission spectrometry. A reaction equation can be written that gives a good description of this behaviour. The possible influence of $NaNO_3$ and cullet on the formation and fining of television glass has also been investigated.

Philips Tech. Rev. 43, No. 9, 260-268, Sept. 1987

# A mobile system for image bulk storage

L. H. Guildford and B. D. Young

*There are many kinds of video signals besides those from television. Many other kinds of systems produce images from sensors; they range from infrared surveillance systems to X-ray diagnostic equipment. Sometimes it is essential to be able to record signals for later analysis off-site. This requires far more elaborate equipment for image bulk storage than an ordinary video recorder. Recently at Philips Research Laboratories hardware and software have been developed to cope with the many possible eventualities. The instrumentation is in fact a complex system that constitutes a complete transportable laboratory.*

## Introduction

Television cameras, night-viewing systems, infrared surveillance systems, ultrasound systems, radar, sonar, X-ray diagnostic equipment — these all produce images from sensor systems. The images have to be processed for simple display, to activate further systems or perhaps to provide a better understanding of the observations or of the operation of the actual system.

Experiments in real-time image processing with such systems are often desirable, but there are problems. The actual scene itself may be unique and economically unrepeatable, taking place in difficult environmental conditions. The image might for example be due to a low-flying aircraft detected and tracked by infrared sensors in unusual weather conditions. It could come from an X-ray medical investigation, where the patient's discomfort should be kept as brief as possible.

It is therefore highly desirable to record the video information from the sensors on the spot. Then the images can be recreated, studied and processed at will later. The recording must be such that high-quality unadulterated video information from the sensor system is readily available.

Ultimately there are various options: the information may be viewed directly as a two-dimensional picture, plotted as a graph or perhaps used as the basic data for the recognition of a characteristic pattern (an 'object signature') to trigger automatic reaction by a system.

*L. H. Guildford, M.I.E.R.E., was formerly with Philips Research Laboratories, Redhill, Surrey, England; B. D. Young, B.Sc., A.M.I.E.E., is with these laboratories.*

Collecting and recording the video signals from different types of sensor systems requires a sophisticated image bulk store with the appropriate equipment for preprocessing and postprocessing. Such a storage system including all the ancillary hardware forms the subject of this article. The system is designed for monochrome ('black and white') images only.

## Image signal characteristics

Some of the sensor systems listed above will present information as a signal that is compatible with the international CCIR standards for television [1]. Others make use of more unusual scene-scanning formats. In general these will be line-scanning structures based on rectilinear formats (as in television, but with different parameter values), radial line scans (as in radar) or vertical line scans swept horizontally to produce a 360° 'cylindrical' scan for omnidirectional surveillance.

The signals from the sensors will often be in analog form, sometimes with synchronization pulses interleaved with the video signals proper, thus producing composite waveforms. Sometimes, however, video and synchronization signals are provided on separate connections. Digitized signals supplied directly from the sensors will become more common in future. This means that our system for image bulk storage must be capable of dealing with both analog and digital signal formats and with a wide variety of scan-synchronization signals.

However the signals from the sensors are to be displayed or used, certain operational parameters always

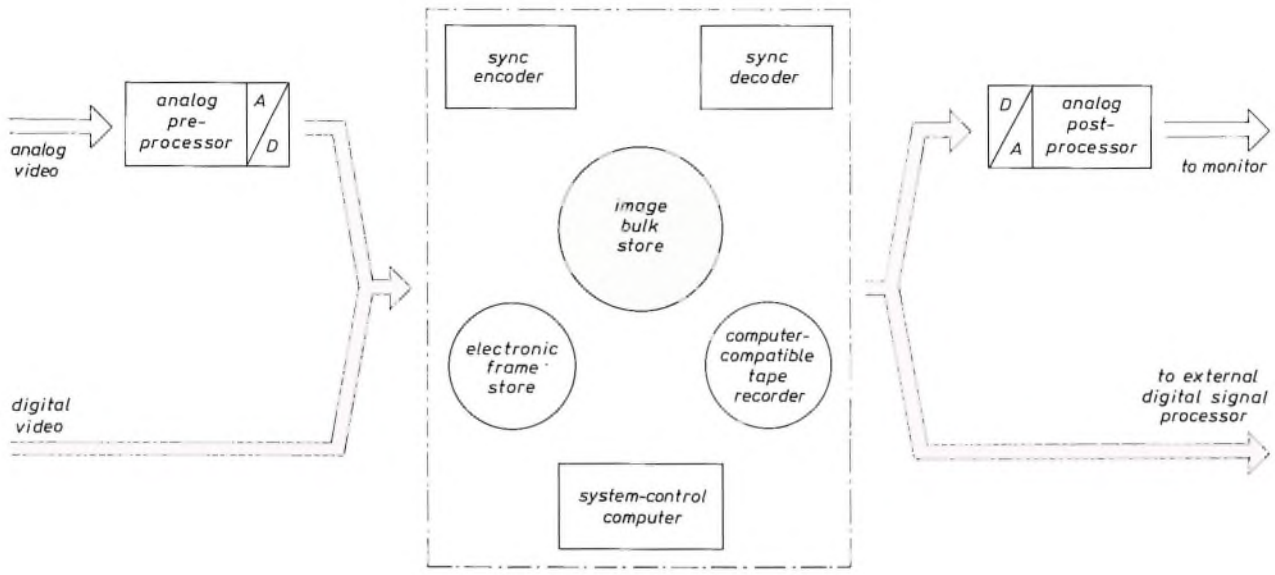


**Fig. 1.** Basic functional diagram of the mobile system for image bulk storage. The system consists of a number of subsystems that can be interconnected in a variety of ways to suit the particular needs of the user. All signal processing is basically digital. Analog video signals are therefore first converted to digital and back to analog after processing. The actual image bulk store is a 24-track tape recorder. An electronic frame store and a computer-compatible tape recorder are also available. For synchronization purposes special encoder and decoder circuits have been designed. The entire system is controlled from the system-control computer.

have to be established and maintained for recording and analysing the information.

- A zero reference level for the video signal (the 'black level'). This can be either absolute or related to the scene.
- The dynamic range for the signal from the sensors. This is normally expressed as the range between the black level, as a reference value, and the peak level representing white.
- The resolution of the signal. Two kinds of resolution are significant: the spatial resolution in terms of the number of picture elements (pixels) or samples within a given image region, and the amplitude resolution in terms of signal-to-noise ratio, minimum detectable signal or number of bits per sample.
- The system characteristics of the overall system from the output of the sensors to the point of measurement. They should be linear and the corresponding frequency response should be as flat as possible.

For infrared systems the dynamic range of the video signal can be greater than 60 dB (an amplitude ratio of 1000:1, requiring at least 10 bits per sample), but mostly a dynamic range of 48 dB (an amplitude ratio of 250:1, requiring at least 8 bits per sample) is sufficient.

For monochrome television signals a sampling rate of about 12 MHz is necessary. In processing the signals of other image-sensing applications of interest sampling rates as high as 18 MHz can occur, especially when two or more signals are combined in time-division multiplex to allow a number of different sensor devices to view the same scene simultaneously.

All the normal scan formats produce some degree of 'dead time' in which no video information is produced. For instance, the scanning formats used with standard television systems allow approximately 20% of the time for scan flyback. Infrared scanners with optomechanical scanning often produce as much as 50% of dead time. By storing and reformatting the incoming information, the effective bandwidth required of a recording medium can be reduced. It is also possible to reduce the amount of storage required per frame, if the information relating to the dead times is kept to the absolute minimum.

## System requirements

From the outset we wanted our system for image bulk storage to meet the following basic requirements.

- It must make a high-quality record of incoming images.
- It must enable the replay of recorded information at the original recording speed and at various much lower speeds.

[1] Report No. 308-2, Characteristics of monochrome television systems, Proc. XIIth CCIR Plenary Assembly, Vol. V, pt. 2, New Delhi 1970 (published by the ITU, Geneva 1970);
Report No. 624-2, Characteristics of television systems, Recommendations and reports of the CCIR, Vol. XI, pt. 1, Broadcasting service (television), ITU, Geneva 1982.

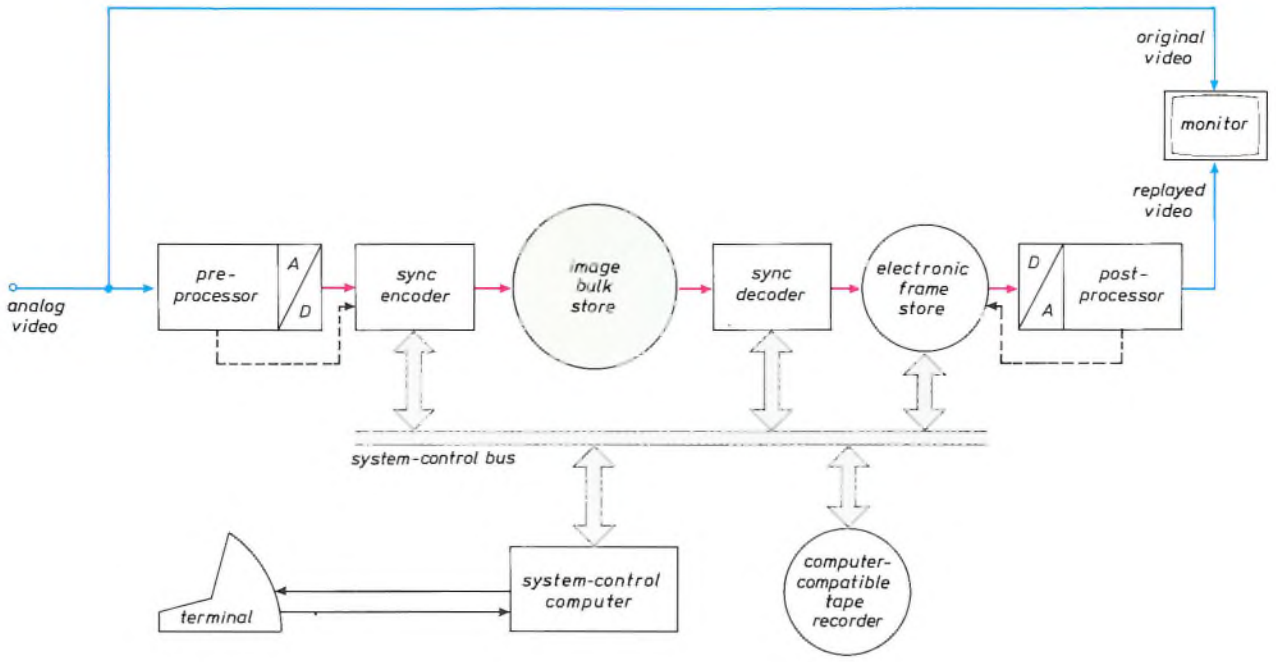


**Fig. 2.** System configuration for storing standard analog television signals. After analog preprocessing and A/D conversion the sync encoder replaces the conventional sync information by digital information for both synchronization and image-identification purposes. The signal is then stored in the image bulk store. On replay individual frames are stored in the frame store. They can be transferred to the computer-compatible tape recorder for further off-line processing or they can be viewed on a monitor after D/A conversion and appropriate postprocessing. Connections intended for synchronization purposes are indicated by dashed lines. The system is controlled from a computer terminal via the system-control computer and the system-control bus.

- It must be possible to obtain still pictures ('frozen frames'), so that information can be examined frame by frame.
- It must include a computer-compatible tape recorder (with 1/2-inch tape) for recording a selected still picture. Recorded images can then be analysed off-line by an external computer, manipulated as required within that computer and replayed at will for further use.
- The hardware of the complete system must be self-contained and transportable.

Now that the image signal characteristics, described in the previous section, are known the basic functional diagram of *fig. 1* can be derived; it shows the individual modules required. Because the main functions are executed digitally any analog video input signal is first preprocessed and converted to digital. Similarly any analog video output signal is obtained from the system after digital-to-analog conversion and post-processing. The heart of the system consists of three storage media:

- an electronic store that can contain two television frames at a time,
- an image tape recorder, which constitutes the actual image bulk store, and
- a computer-compatible tape recorder that serves as an output device enabling external processing later, e.g. on a mainframe computer.

As we are dealing with video signals, synchronization is an important aspect of the interaction of input devices, output devices and storage media. Two separate units indicated by 'sync encoder' and 'sync decoder' are provided for this purpose.

The system-control computer is used to set up and monitor all operations.

## System architecture

The modules of fig. 1 are deliberately shown without interconnections; depending on the particular application of the system the modules may be connected in many different ways. For instance, the frame store may be placed either before or after the bulk store or not used at all. There are many possible configurations to suit the user's needs, both for recording and replaying television or non-standard image formats. All modules have therefore been made plug-compatible at their interfaces so that they can easily be patched together to produce a great variety of recording and replay functions.

One specific system configuration with its interconnections is shown in *fig. 2*. This configuration can be used for processing a standard analog television signal. After preprocessing, A/D conversion and sync encoding the signal is recorded digitally in the bulk store. On replaying the video recording the signal passes through the sync decoder, is reformatted in the frame store and after subsequent D/A conversion and postprocessing is replayed on a television monitor. Alternatively individual frames may be selected for detailed examination on the monitor or recorded on the computer-compatible tape recorder.

Some particular features of this configuration are:

- the monitor can display either the original or the replayed video signal;


**Fig. 5.** Loading the mobile laboratory on to a transporter.

**Fig. 3.** System hardware under test in the laboratory. From left to right: preprocessing and postprocessing rack with monitor; system-control computer and computer-compatible tape recorder; 24-track digital image tape recorder (the actual image bulk store); electronics of digital image tape recorder in combination with sync encoder and sync decoder; electronic frame store control console.

**Fig. 4.** The system hardware installed in a container forms a mobile laboratory.

- the image bulk store can be by-passed, which means that the system can be set up and tested without actually running the bulk tape;
- when incoming signals are being recorded, the replay circuits are also operational permitting the recorded information to be continuously monitored.

An impression of the actual hardware can be obtained from figs 3 to 5. In *fig. 3* a laboratory arrangement for testing is shown. All modules and some additional equipment for heating, lighting, power supply, dust filtering etc. have been installed in a thermally insulated container (*fig. 4*). The resulting mobile laboratory is transportable as can be seen from *fig. 5*.

Now let us consider the operation of the individual modules in some more detail.

## System modules

### *The preprocessor*

The input signal to the preprocessor (*fig. 6*) is assumed to be an analog video signal with a peak-to-peak amplitude of 1 V and with the zero level corresponding to 'black' (it is 'black-level clamped'). The chief tasks of the analog preprocessor are to remove and separate the synchronization signals, to normalize the remaining video signal to the range $(-0.5\ \text{V}, 0.5\ \text{V})$ and to generate clock pulses for the A/D conversion. (By normalizing the video-signal amplitude and removing the synchronization signals before A/D conversion, the input range of the A/D converter is fully exploited.) The preprocessor also comprises the anti-aliasing filter that is required to prevent 'fold-over' distortion in the A/D conversion [2]. The sampling

[2] See for example pp. 135-136 in: A. W. M. van den Enden and N. A. M. Verhoeckx, Digital signal processing: theoretical background, Philips Tech. Rev. 42, 110-144, 1985.

times for the A/D converter are determined by the clock pulses which can be made to appear regularly between 1 and 1024 times during each line time. The output samples (each corresponding to one pixel) have the form of binary words consisting of 8 bits in parallel. The maximum sampling rate is 15 MHz.

In the preprocessor the composite sync signal that is stripped from the incoming video is separated into a line sync signal that has a short pulse at the start of each line and a frame sync signal that has a long pulse at the start of each television field.

### *The sync encoder*

The main task of the sync encoder is the insertion of digitally encoded sync information (the 'sync code block') into the stream of video samples to be presented to the image bulk store. The sync code block consists of 16 successive 8-bit words ('bytes') that can easily be inserted between the 8-bit video samples. This is done at the beginning of each line period. One part of the sync code block (16 bits) is always the same and characterizes the occurence of the block. A second part (16 bits) represents a frame number; an increase of this number by one indicates the start of a new frame. A third part (48 bits) can be used in an arbitrary way for identifying a series of frames and is therefore called the 'frame title'; these titles can be keyed in from the system-control computer. The remaining 48 bits are redundant and can provide added protection against errors.

### *The image bulk store*

The heart of our system is the image bulk store. It is a commercially available 24-track digital magnetic tape recorder capable of recording and replaying binary sig-

#### *Typical sync code block structure*

A typical 16-byte sync code block is shown in *fig. 7*. The 16 bytes are numbered 0, 1, 2, ..., 15 and the 8 bits of each byte are numbered 0, 1, 2, ..., 7. The pattern of zeros and ones for bit 0 is the same for each sync code block; bits 1, 2 and 3 constitute the 48-bit frame title. The combination of bits 4 to 7 of bytes 2, 6, 10 and 14 yield the frame number (in this case: 0101 1000 0111 0000 = 22640). In all the other bytes the bits 4 to 7 are 'inverted reflected' versions of bits 0 to 3. They carry redundant information for error checking.

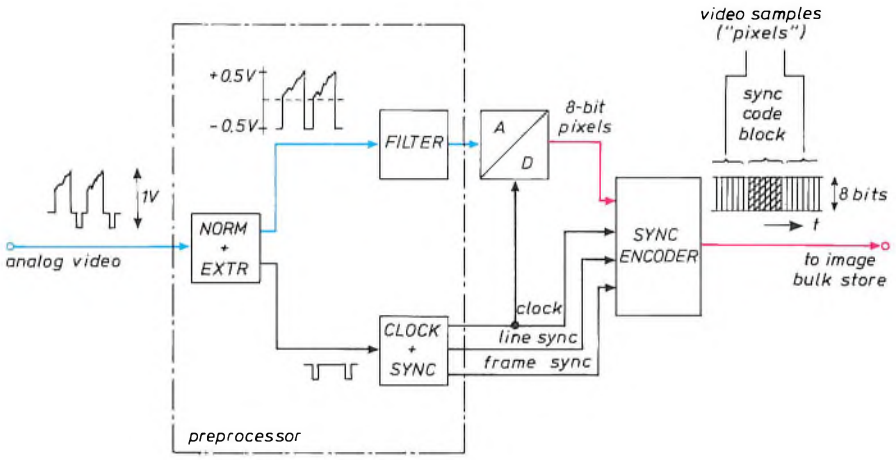


**Fig. 6.** Block diagram of the main circuits that are active during recording in the configuration of fig. 2. *NORM+EXTR* circuits for normalization of the video signal amplitude and extraction of sync signals. *FILTER* anti-aliasing filter inserted in front of the A/D converter. *CLOCK+SYNC* tunable clock generator determining the sampling rate of the A/D converter (= pixel rate) and generator of line-sync signals and frame-sync signals.

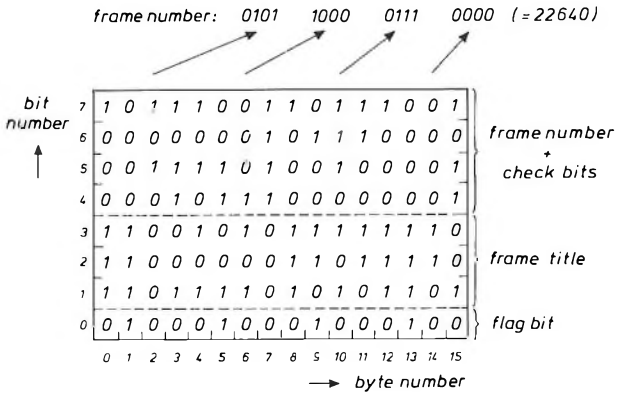


**Fig. 7.** Typical sync code block consisting of 16 bytes of 8 bits.

nals at rates from 0 to 3.3 Mbit/s on each track. As our video samples ('pixels') consist of 8 bits three samples can be recorded in parallel and we can accomodate $9.9 \times 10^6$ video samples per second in a straightforward way. By exploiting the 'dead times' that occur in almost any video information (p. 261) we can increase the effective recording rate. The incoming video samples are therefore stored and reformatted frame by frame in the frame store before recording. The inverse process must then be applied on replay.

### *The sync decoder*

When the sync decoder is presented with an 8-bit parallel data stream from the image bulk store on replay, it will look for sync codes as described above. If a code block is detected the sync decoder will issue a line sync pulse, and if an increment of the frame number by 1 is observed a frame sync pulse is generated (*fig. 8*).

Initially the sync decoder is programmed from the system-control computer via the system-control bus with the frame title of the required frame. In the decoder the correlation between the actual incoming data stream and the reference title is examined continuously. This is done at the full sampling rate (hence at a rate of 9.9 MHz). The redundant bits in the sync code are also checked. The results of these two measurements need not yield 100% agreement, but should exceed certain preset thresholds that allow for some tape drop-outs that might occur in a code block. Once the sync code block has been detected, the detector is inactive for almost the entire estimated duration of a line period ('temporal filtering' or 'time windowing'). A time window is applied to the frame synchronization in a similar way.

#### *Individual frame selection*

To provide the ability to select any particular frame for storage in the frame store a comparator circuit in the sync decoder can be programmed to search for a specific frame number. On detection of this number, frame-sync generation is inhibited, thus preventing further updates of the frame store. This facility is particularly useful when a set of sequential images is required for off-line analysis on a mainframe computer.

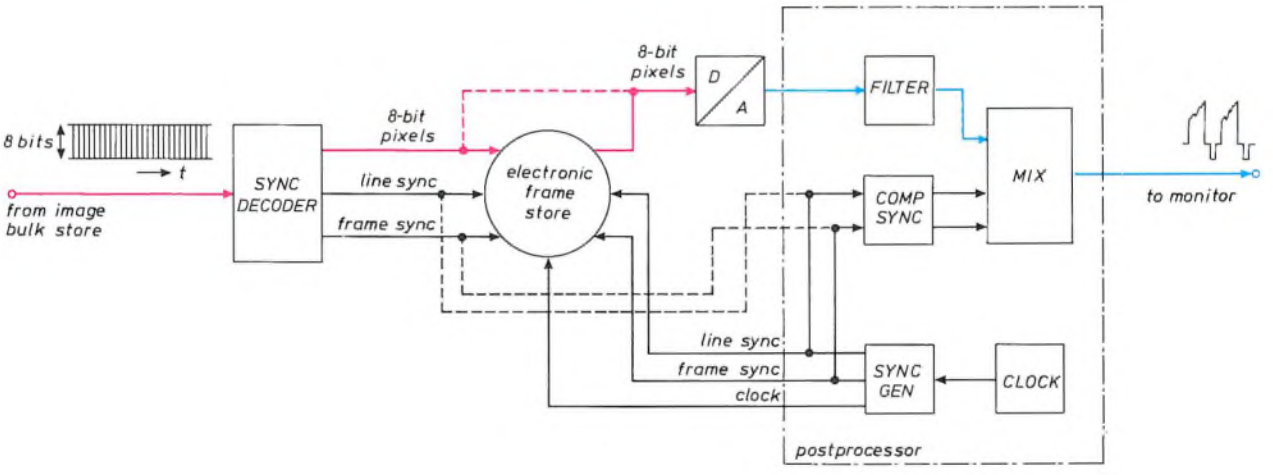


**Fig. 8.** Block diagram of the main circuits that are active during replay in the configuration of fig. 2. *CLOCK* tunable clock generator determining the pixel rate. *SYNC GEN* generator of line-sync signals and frame-sync signals. *COMP SYNC* circuit for generating composite sync signal and blanking signal. *MIX* circuit for combining the analog video signal (obtained after D/A conversion and lowpass filtering) with the composite sync signal and the blanking signal. The postprocessor can be connected directly to the sync decoder (dashed lines) when the frame store is not used.

### *The frame store*

The frame store is one of the key components that makes the overall system so versatile; it can be positioned at many different locations in the system configuration for performing many kinds of buffering and reformatting operations. As a consequence the frame store itself is a rather complicated subsystem, and only its most important features will be mentioned here.

The frame store (*fig. 9*) is a dedicated piece of hardware, designed at our Laboratories. It is a random-access memory (RAM) with a capacity of approximately half a million 12-bit words (as our pixels are

represented by 8-bit words, 4 bits of each word are not actually used at present). The memory is organized into two separate pages that can each store 512 × 512 12-bit words. Each page constitutes a complete video frame. In the fastest addressing mode (the 'linear addressing mode') data words can be written into the store at a rate of 18.6 MHz and read out at a maximum rate of 15.6 MHz.

To achieve independence between read and write accesses, the store has individual read and write ports serviced by their own address generators.

The frame store has a single-board microcomputer. Its control console provides the user with local, stand-alone operation of the frame store for manual data entry and control of the address generators. The microcomputer is also connected to the system-control bus, interpreting and controlling communication between the system computer and the frame store. By programming the correct sequences of addresses used in writing and reading, we can let the frame store perform many types of formatting operations on the stored video information.

The frame store itself is built up from 16 parallel segments, each comprising 32k (= $2^{15}$) 12-bit words of dynamic memory. In each segment a combined read/write cycle can be performed in 800 ns corresponding to a maximum update rate of 1.25 MHz. Internal sequential access to all 16 segments gives a theoretical maximum overall update rate of 20 MHz. For this sequential access 4 bits are required both at the input and at the output of the 16 segments; to compensate for the internal delay in the segments a small 'read segment delay' is provided as indicated in fig. 9.

As the operation of the dynamic memory is asynchronous to the memory accesses, extensive data buffering is employed at the input and output parts of the memory (not shown explicitly in the figure).

*The postprocessor*

The final operations necessary for obtaining a common composite video output signal from our system are performed in the postprocessor (fig. 8). These include both analog filtering, required for signal reconstruction after D/A conversion, and the insertion of combined line and frame-sync signals into the video signal. The postprocessor therefore has a pixel clock generator and various circuits for generating the correct sync and blanking signals. When the frame store is used, the reading process of the store is 'slaved' to the sync signals of the postprocessor (while the writing process is under the control of the sync decoder). If the frame store is not used, the synchronization of the postprocessor can be slaved to the sync decoder (indicated by dashed lines).

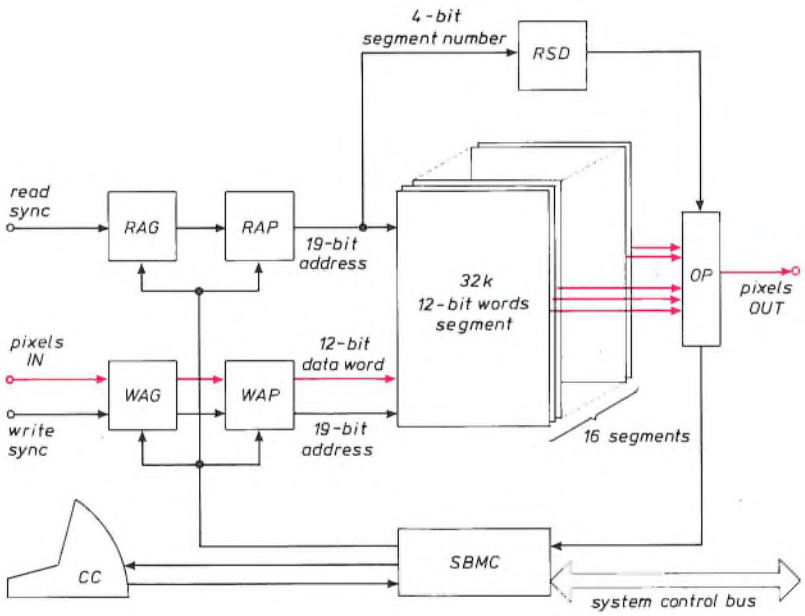


**Fig. 9.** Frame-store schematic diagram. The store consists of 16 parallel segments of dynamic memory, each segment comprising 32k of 12-bit words. *RAG* read address generator. *RAP* read-access port. *WAG* write address generator. *WAP* write-access port. *RSD* read segment delay. *OP* output port. *SBMC* single-board microcomputer. *CC* control console.

*The system-control computer*

The system-control computer is a commercially available piece of hardware (Texas Instruments 990/4) that gives the user control over many of the programmable features of our image bulk-storage system. Among these are the following facilities:

- choice of master-clock frequency between 873 kHz and 25 MHz;
- programming of address patterns for the frame store;
- choice of sync code, including the 48 bits for frame titles;
- transfer of video data from the frame store to the computer-compatible tape recorder or vice-versa;
- execution of various types of tests on parts of the system;
- storage on computer disk of particular system parameter settings that can be used for setting up the system or examined on print-out.

## Application examples

From the many possible applications of our image bulk-storage system we have chosen one particular example that clearly demonstrates a number of important features. The picture information that we start with in this case originates from a system called IRSCAN. This is an omnidirectional (360°) infrared surveillance system that has a vertical angle of view of 4°. It uses a vertical line-scanning pattern comprising 16384 lines in one complete rotation, which takes 0.5 s. This scanning format is symbolically represented in *fig. 10a*.

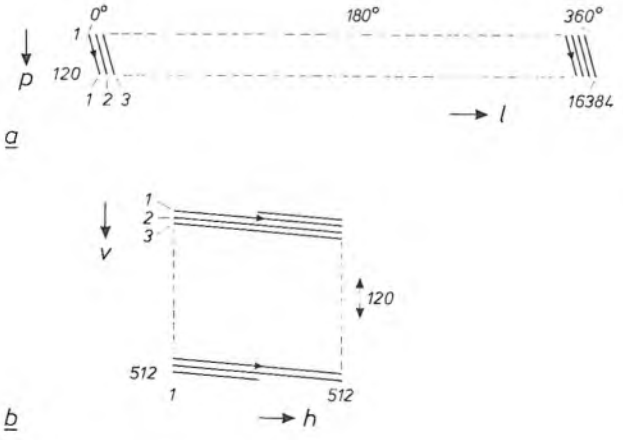


**Fig. 10.** *a*) Scanning format in the omnidirectional infrared surveillance system IRSCAN. There are 16384 vertical scanning lines in each complete rotation (360°). At A/D conversion 120 pixels are derived from each line. *p* pixel number, *l* line-scan number in the IRSCAN system. *b*) After storage in the (512 × 512)-pixel frame store and reformatting, a part of the IRSCAN image can be displayed on a monitor using the standard horizontal scanning format. The blue area in the upper drawing is then represented as the blue area in the lower diagram. *v* vertical address number of the frame store corresponding to the line number in standard television, *h* horizontal address number of the frame store determining the horizontal position on the standard television monitor.

Our storage system can be used to replay pictures or parts of pictures from this surveillance system on a standard television monitor for analysis. Each vertical line in the IRSCAN signal is first converted into 120 pixels, each represented by an 8-bit word. Before recording on the image bulk-store tape recorder, each group of 120 pixels is augmented by a sync code block containing information about the line number and the particular azimuth scan number.

On replay, any part of an IRSCAN picture consisting of 512 lines (blue area in fig. 10*a*) is written into the frame store while a vertical line addressing format is used. For read-out from this store a horizontal line addressing format is used, corresponding to a standard television scan. In this way the contents of the frame store can be displayed in the blue area of the television screen, schematically represented in fig. 10*b*. (In practice certain operations related to the usual interlacing also have to be incorporated into the addressing format of the store.) In the frame store parts of different pictures can also be combined for simultaneous display, permitting the comparison of different pictorial aspects.

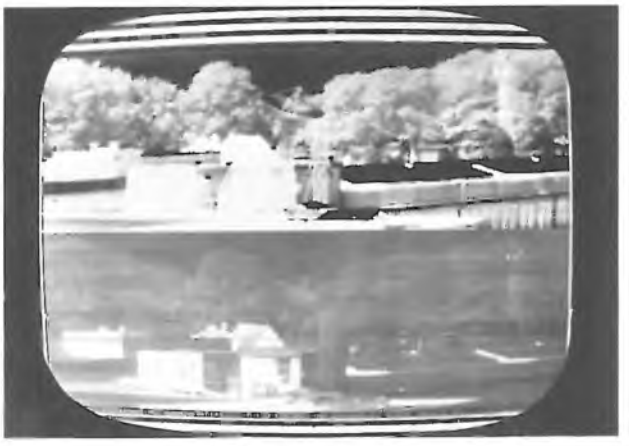

**Fig. 11.** An application of the image bulk-storage system. Here two optically coincident infrared images from the IRSCAN system are combined on one television screen. The upper image displays information obtained at wavelengths of 8 to 14 μm; the lower image represents wavelengths of 3 to 5 μm.

Some practical results are shown in figs 11 and 12. In *fig. 11* two coincident infrared images of the same scene are shown one on top of the other on one

**Fig. 12.** Sometimes it is very useful to compare images obtained from the same scene by different methods using the image bulk-storage system. Here an optical image (top) and an infrared image (bottom) of the same outdoor scene are displayed simultaneously on two monitors.

screen. The upper image has been made with an infrared detector for wavelengths of 8 to 14 μm, the lower image with a detector for wavelengths of 3 to 5 μm. The upper image is saturating on highlights due to excessive temperature differentials in the scene.

A second example is given in *fig. 12*. The upper photograph shows an ordinary video image of an outdoor scene and the lower photograph shows an infrared picture of the same scene; useful information can often be gathered from a comparison of such pairs of images.

**Summary.** Often the value of image signals obtained from sources such as TV cameras, night-viewing systems, infrared sensors, ultrasound systems, X-ray equipment and so on, is increased considerably if the images can be recorded faithfully for later analysis or processing. Unfortunately the signal characteristics (e.g. the scanning format) in all these cases can vary greatly. To cope with this variety a versatile system for image bulk storage has been designed around a standard 80-Mbit/s 24-track digital tape recorder. The images can be reformatted either before or after recording by means of an electronic frame store. Images can be replayed on a standard TV monitor or copied on to a computer-compatible magnetic tape for further off-line processing on a mainframe computer. A control computer manages system operation. The application of a sync-block coding scheme permits easy identification and selection of individual images. The image bulk-storage system constitutes a complete transportable laboratory housed in a standard (6.7 m × 2.4 m) shipping container.

# Scientific publications

These publications are contributed by staff from the laboratories and other establishments that form part of or are associated with the Philips group of companies. Many of the articles originate from the research laboratories named below. The publications are listed alphabetically by journal title.

Philips GmbH Forschungslaboratorium Aachen, Weißhausstraße, 5100 Aachen, Germany — *A*

Philips Research Laboratory, Brussels, 2 avenue Van Becelaere, 1170 Brussels, Belgium — *B*

Philips Natuurkundig Laboratorium, Postbus 80 000, 5600 JA Eindhoven, The Netherlands — *E*

Philips GmbH Forschungslaboratorium Hamburg, Vogt-Kölln-Straße 30, 2000 Hamburg 54, Germany — *H*

Laboratoires d'Electronique et de Physique Appliquée, 3 avenue Descartes, 94450 Limeil-Brévannes, France — *L*

Philips Laboratories, N.A.P.C., 345 Scarborough Road, Briarcliff Manor, N.Y. 10510, U.S.A. — *N*

Philips Research Laboratories, Cross Oak Lane, Redhill, Surrey RH1 5HA, England — *R*

Philips Research Laboratories Sunnyvale P.O. Box 9052, Sunnyvale, CA 94086, U.S.A. — *S*

| | | | | |
|---|---|---|---|---|
| M. L. Verheijke *E* | Toepassing van neutronenactiveringsanalyse, autoradiografie en radioactieve tracers in de siliciumtechnologie | Anal. Techn. **7** | 30-34 | 1986 |
| J. Zhang (*Imp. College, London*), J. H. Neave, P. J. Dobson & B. A. Joyce *R* | Effects of diffraction conditions and processes on RHEED intensity oscillations during the MBE growth of GaAs | Appl. Phys. A **42** | 317-326 | 1987 |
| M. Delfino, D. K. Sadana & A. E. Morgan *S* | Shallow junction formation by preamorphization with tin implantation | Appl. Phys. Lett. **49** | 575-577 | 1986 |
| P. Rutérana, P. Friedel, J. Schneider & J. P. Chevalier (*C.E.C.M.-C.N.R.S., Vitry*) *L* | High resolution electron microscopy of the GaAs/$Si_3N_4$ interface produced by multipolar plasma deposition | Appl. Phys. Lett. **49** | 672-673 | 1986 |
| H. van Houten, B. J. van Wees (*Delft Centre for Submicron Technol., Delft*), M. G. J. Heijman & J. P. André *E, L* | Submicron conducting channels defined by shallow mesa etch in GaAs-AlGaAs heterojunctions | Appl. Phys. Lett. **49** | 1781-1783 | 1986 |
| S. Makram-Ebeid, P. Boher & M. Lannoo (*ISEN, Lille*) *L* | Interactions between bombardment-induced defects in GaAs | Appl. Phys. Lett. **50** | 270-272 | 1987 |
| J. J. P. Bruines, R. P. M. van Hal, B. H. Koek, M. P. A. Viegers & H. M. J. Boots *E* | Between explosive crystallization and amorphous regrowth: inhomogeneous solidification upon pulsed-laser annealing of amorphous silicon | Appl. Phys. Lett. **50** | 507-509 | 1987 |
| J. Maguire*, R. Murray*, R. C. Newman* (**J. J. Thomson Phys. Lab., Whiteknights*), R. B. Beall & J. J. Harris *R* | Mechanism of compensation in heavily silicon-doped gallium arsenide grown by molecular beam epitaxy | Appl. Phys. Lett. **50** | 516-518 | 1987 |
| J. W. M. Bergmans & Y. C. Wong *E* | A simulation study of intersymbol interference cancellation | Arch. Elektron. & Uebertragungstech. Bd. 41 | 33-37 | 1987 |
| J. Jerrams-Smith (*Univ. Birmingham*) *R* | An expert system within a supportive interface for UNIX | Behav. & Inf. Technol. **6** | 37-41 | 1987 |
| R. Waser *A* | Diffusion of hydrogen defects in $BaTiO_3$ ceramics and $SrTiO_3$ single crystals | Ber. Bunsenges. Phys. Chem. **90** | 1223-1230 | 1986 |
| W. Hermann, A. Raith & H. Rau *A* | Diffusion of fluorine in silica | Ber. Bunsenges. Phys. Chem. **91** | 56-58 | 1987 |
| P. H. L. Notten *E* | The role of surface charging and potential redistribution on the kinetics of hole injection reactions at *n*-GaAs | Electrochim. Acta **32** | 575-581 | 1987 |
| G. M. Loiacono *N* | Crystal growth of $KH_2PO_4$ | Ferroelectrics **71** | 49-60 | 1987 |

| | | | | | |
|---|---|---|---|---|---|
| A. Bhattacharyya, J. D. Reimer & K. N. Ritz *S* | Breakdown voltage characteristics of thin oxides and their correlation to defects in the oxide as observed by the EBIC technique | IEEE **EDL-7** | 58-60 | 1986 |
| F. L. van Nes (*Inst. Perception Res., Eindhoven*) | A new teletext character set with enhanced legibility | IEEE Trans. **ED-33** | 1222-1225 | 1986 |
| A. Bhattacharyya & S. N. Shabde *S* | Degradation of short-channel MOSFET's under constant current stress across gate and drain | IEEE Trans. **ED-33** | 1329-1333 | 1986 |
| A. W. Ludikhuize *E* | A versatile 250/300-V IC process for analog and switching applications | IEEE Trans. **ED-33** | 2008-2015 | 1986 |
| P. Piret *B* | Bounds for codes over the unit circle | IEEE Trans. **IT-32** | 760-767 | 1986 |
| P. Delsarte & P. Piret *B* | Do most binary linear codes achieve the Goblick bound on the covering radius? | IEEE Trans. **IT-32** | 826-828 | 1986 |
| P. van Weijer *E* | Pulsed optical pumping as a tool for the determination of population mechanisms of excited states in a low-pressure mercury discharge | IEEE Trans. **PS-14** | 464-470 | 1986 |
| A. G. Dirks, T. Tien & J. M. Towner *S* | Al-Ti and Al-Ti-Si thin alloy films | J. Appl. Phys. **59** | 2010-2014 | 1986 |
| K. N. Ritz, M. Delfino, C. B. Cooper III* & R. A. Powell* (**Varian Res. Center, Palo Alto, CA*) *S* | Observation of slip dislocations in (100) silicon wafers after $BF_2$ ion implantation and rapid thermal annealing | J. Appl. Phys. **60** | 800-802 | 1986 |
| J. Khurgin, B. J. Fitzpatrick & W. Seemungal *N* | Cathodoluminescence, gain, and stimulated emission in electron-beam-pumped ZnCdSe | J. Appl. Phys. **61** | 1606-1609 | 1987 |
| G. J. van Gurp, P. R. Boudewijn, M. N. C. Kempeners & D. L. A. Tjaden *E* | Zinc diffusion in *n*-type indium phosphide | J. Appl. Phys. **61** | 1846-1855 | 1987 |
| P. J. Schoenmakers, F. C. C. J. G. Verhoeven & H. M. van den Bogaert *E* | Application of supercritical fluid chromatography to the analysis of liquid-crystal mixtures | J. Chromatogr. **371** | 121-134 | 1986 |
| P. J. Schoenmakers & T. Blaffert *E,H* | Effect of model inaccuracy on selectivity optimization procedures in reversed-phase liquid chromatography | J. Chromatogr. **384** | 117-133 | 1987 |
| C. Guedon, J. Le Bris & J. L. Gentner *L* | Control of interface formation during growth of InGaAs/InP heterostructures by chloride vapour phase epitaxy | J. Cryst. Growth **79** | 909-913 | 1986 |
| E. P. Menu, D. Moroni, J. N. Patillon, T. Ngo & J. P. André *L* | High mobility of two-dimensional electrons in $Ga_{1-x}In_xAs/InP$ heterostructures grown by atmospheric pressure MOVPE | J. Cryst. Growth **79** | 920-927 | 1986 |
| P. J. Dobson, B. A. Joyce, J. H. Neave & J. Zhang (*Imp. College, London*) *R* | Current understanding and applications of the RHEED intensity oscillation technique | J. Cryst. Growth **81** | 1-8 | 1987 |
| J. Aarts, W. M. Gerits & P. K. Larsen *E* | Monolayer and bilayer growth on Ge(111) | J. Cryst. Growth **81** | 65-66 | 1987 |
| P. F. Fewster, J. P. Gowers, D. Hilton & C. T. Foxon *R* | Structural studies of GaAs-AlAs superlattices grown by MBE | J. Cryst. Growth **81** | 120 | 1987 |
| K. Woodbridge, J. P. Gowers, P. F. Fewster, J. H. Neave & B. A. Joyce *R* | RHEED studies and interface analysis of GaAs grown on Si(001) | J. Cryst. Growth **81** | 224-225 | 1987 |
| E. T. J. M. Smeets *E* | Solid composition of $GaAs_{1-x}P_x$ grown by organometallic vapour phase epitaxy | J. Cryst. Growth **82** | 385-395 | 1987 |
| A. H. van Ommen, M. F. C. Willemsen, A. E. T. Kuiper & F. H. P. M. Habraken (*Univ. Utrecht*) *E* | Etch rate modification of $Si_3N_4$ layers by ion bombardment and annealing | J. Electrochem. Soc. **131** | 2140-2147 | 1984 |
| E. K. Broadbent, A. E. Morgan, J. M. DeBlasi, P. van der Putte, B. Coulman, B. J. Burrow, D. K. Sadana & A. Reader *E,S* | Growth of selective tungsten on self-aligned Ti and PtNi silicides by low pressure chemical vapor deposition | J. Electrochem. Soc. **133** | 1715-1721 | 1986 |
| M. Delfino, D. K. Sadana, A. E. Morgan & P. K. Chu (*C. Evans & Associates, San Mateo, CA*) *S* | A study of atomic and molecular arsenic ion-implanted silicon | J. Electrochem. Soc. **133** | 1900-1905 | 1986 |

| | | | | | |
|---|---|---|---|---|---|
| P. H. L. Notten & J. J. Kelly | *E* | Evidence for cathodic protection of crystallographic facets from GaAs etching profiles | J. Electrochem. Soc. **134** | 444-448 | 1987 |
| D. M. de Leeuw, T. Kovats & S. P. Herko | *N* | Kinetics of photostimulated luminescence in BaFBr:Eu | J. Electrochem. Soc. **134** | 491-493 | 1987 |
| P. K. Bachmann, P. Geittner, D. Leers & H. Wilson | *A* | Loss reduction in fluorine-doped SM- and high N.A.-PCVD fibers | J. Lightwave Technol. **LT-4** | 813-817 | 1986 |
| P. Geittner, H. J. Hagemann, J. Warnier & H. Wilson | *A* | PCVD at high deposition rates | J. Lightwave Technol. **LT-4** | 818-822 | 1986 |
| P. K. Bachmann, D. Leers, H. Wehr, D. U. Wiechert, J. A. van Steenwijk, D. L. A. Tjaden & E. R. Wehrhahn (*Philips Kommunikations Industrie, Nürnburg*) | *A,E* | Dispersion-flattened single-mode fibers prepared with PCVD: performance, limitations, design optimization | J. Lightwave Technol. **LT-4** | 858-863 | 1986 |
| H. J. G. Draaisma*, W. J. M. de Jonge* (**Univ. of Technol., Eindhoven*) & F. J. A. den Broeder | *E* | Magnetic interface anisotropy in Pd/Co and Pd/Fe multilayers | J. Magn. & Magn. Mater. **66** | 351-355 | 1987 |
| A. Bhattacharyya & C. Vorst | *S* | Effect of addition of TCA (trichloroethane) on the electrical properties of thin oxides processed by a two-step oxidation technique | J. Phys. D **19** | L161-L166 | 1986 |
| M. J. Keesman, P. H. G. Offermans & E. P. Honig | *E* | Silica gel formation followed by dynamic shear experiments | Mater. Lett. **5** | 140-142 | 1987 |
| M. Delfino & P. K. Chu (*C.Evans & Associates, San Mateo, CA*) | *S* | Donor creation during oxygen implanted buried oxide formation | Mater. Res. Soc. Symp. Proc. **53** | 245-250 | 1986 |
| G. J. Campisi, H. B. Dietrich (*Naval Res. Lab., Washington, DC*), M. Delfino & D. K. Sadana | *S* | High dose implantation of nickel into silicon | Mater. Res. Soc. Symp. Proc. **54** | 747-752 | 1986 |
| W. G. M. van den Hoek | *S* | The etch mechanism for $AL_2O_3$ in fluorine and chlorine based RF dry etch plasmas | Mater. Res. Soc. Symp. Proc. **68** | 71-78 | 1986 |
| W. G. M. van den Hoek | *S* | Characterization of plasma-enhanced chemical vapour deposition of silicon-oxynitride | Mater. Res. Soc. Symp. Proc. **68** | 335-342 | 1986 |
| J. M. DeBlasi, D. K. Sadana & M. H. Norcott | *S* | Interfacial tunnel structures in CMOS source/drain regions following selective deposition of tungsten | Mater. Res. Soc. Symp. Proc. **71** | 303-308 | 1986 |
| S. Aronowitz* & M. Delfino (**Fairchild Res. Center, Palo Alto, CA*) | *S* | Laser activated glass flow modeling | Mater. Res. Soc. Symp. Proc. **71** | 479-485 | 1986 |
| A. L. J. Burgmans | *E* | IC-technologie op submicron-niveau; een CMOS-proces | Ned. T. Natuurk. A **52** | 99-102 | 1986 |
| F. M. Klaassen | *E* | Fysica van kleine IC-componenten | Ned. T. Natuurk. A **52** | 107-112 | 1986 |
| P. C. Zalm, A. W. Kolfschoten, F. H. M. Sanders & P. Vischer | *E* | Surface processes in ion-induced etching | Nucl. Instrum. & Methods Phys. Res. **B18** | 625-628 | 1987 |
| H. J. Ligthart, E. Gerritsen, P. J. van den Kerkhoff, S. Hoekstra, R. E. van de Leest & E. Keetels | *E* | Aluminium implantations in copper | Nucl. Instrum. & Methods Phys. Res. **B19/20** | 209-212 | 1987 |
| A. H. van Ommen, M. F. C. Willemsen & R. A. M. Wolters | *E* | The effect of ion beam mixing on $MoSi_2$ formation | Nucl. Instrum. & Methods Phys. Res. **B19/20** | 742-745 | 1987 |
| C. W. J. Beenakker | *E* | Evolution of two-dimensional soap-film networks | Phys. Rev. Lett. **57** | 2454-2457 | 1986 |
| M. A. Brummell*, R. J. Nicholas*, M. A. Hopkins* (**Clarendon Lab., Oxford*), J. J. Harris & C. T. Foxon | *R* | Modification of the electron-phonon interactions in GaAs-GaAlAs heterojunctions | Phys. Rev. Lett. **58** | 77-80 | 1987 |
| F. Berz & J. A. Morice | *R* | Accuracy of the transmission coefficient across parabolic barriers as obtained from a generalized WKB approach | Phys. Stat. Sol. b **139** | 573-582 | 1987 |
| J. J. Goedbloed | *E* | Electromagnetic compatibility | Phys. Technol. **18** | 61-67 | 1987 |
| H. W. A. M. Rompa, R. Eppenga & M. F. H. Schuurmans | *E* | Ab initio determinations of oscillator strengths of metals and semiconductors from ASW | Physica **145B** | 5-15 | 1987 |

| | | | | |
|---|---|---|---|---|
| W. F. Druyvesteyn, A. J. M. Kaizer, D. J. Verschuur* & D. de Vries* (**Univ. of Technol., Delft*) *E* | Wigner representation of loudspeaker responses in a living room | Proc. AES Conv., London 1987 (preprint) | 12pp. | 1987 |
| V. Pauker *L* | GaAs monolithic microwave active gyrator | Proc. GaAs IC Symp., Grenelefe, FL, 1986 | 82-85 | 1986 |
| D. Meignant (*RTC Compelec, Limeil-Brévannes*), E. Delhaye & M. Rocchi *L* | A 0.1 - 4.5 GHz, 20 mW GaAs prescaler operating at 125 °C | Proc. GaAs IC Symp., Grenelefe, FL, 1986 | 129-132 | 1986 |
| T. Ducourant, M. Binet, J.-C. Baelde, C. Rocher, J.-M. Gibereau *L* | 3 GHz, 150 mW, 4 bit GaAs analogue to digital converter | Proc. GaAs IC Symp., Grenelefe, FL, 1986 | 209-212 | 1986 |
| P. A. Gough, M. R. Simpson & V. Rumennik *N* | Fast switching lateral insulated gate transistor | Proc. IEDM 86, Los Angeles, CA, 1986 | 218-221 | 1986 |
| S. Mukherjee, C. J. Chou, K. Shaw, D. McArthur & V. Rumennik *N* | The effects of SIPOS passivation on DC and switching performance of high voltage MOS transistors | Proc. IEDM 86, Los Angeles, CA, 1986 | 646-649 | 1986 |
| C. A. M. Mulder & G. Frens *E* | The incorporation of fluorine in vitreous silica | Proc. 1st Int. Workshop on Non-crystalline solids, San Feliu de Guixols 1986 | 259-265 | 1986 |
| J. Hightower, M. Blanco, M. Cagan & K. Monahan *S* | An application of statistical experimental design: comparison of process latitudes for photoresist and cel | Proc. Kodak Microelectron. Seminar, San Diego, CA, 1985 | 39-49 | 1985 |
| U. Schiebel, W. Hillen & T. Zaengel *A* | Image quality in selenium-based digital radiography | Proc. SPIE **626** | 176-184 | 1986 |
| P. J. Severin *E* | Passive components for multimode fibre-optic networks | Proc. SPIE **630** | 98-109 | 1986 |
| M. Erman, N. Vodjdani, P. Jarry, P. Stéphan, J. L. Gentner & C. Guedon *L* | III-V semiconductor waveguides and phase-modulators: the localized vapor phase epitaxy approach | Proc. SPIE **651** | 75-82 | 1986 |
| W. S. Newman & N. Hogan (*Massachusetts Inst. of Technol., Cambridge, MA*) *N* | The optimal control of balanced manipulators | Robotics **3** | 177-184 | 1987 |
| A. G. Dirks & J. J. van den Broek *E* | Precipitation from metastable solid solutions in aluminum rich AL-V thin films | Scr. Metall. **21** | 175-180 | 1987 |
| D. E. Lacklison & P. Capper *R* | Hall effect measurements on Bridgman-grown $Cd_xHg_{1-x}Te$ and their analysis | Semicond. Sci. Technol. **2** | 136-144 | 1987 |
| A. F. Deutz*, H. B. Brom*, H. Deelen*, L. J. de Jongh*, W. J. Huiskamp* (**Univ. Leiden*) & K. H. J. Buschow *E* | Induced-moment ferromagnetic ordering in the singlet ground state compound $TmNi_2$ | Solid State Commun. **60** | 917-921 | 1986 |
| P. W. J. M. Boumans & J. J. A. M. Vrakking *E* | Detection limits of about 350 prominent lines of 65 elements observed in 50 and 27 MHz inductively coupled plasmas (ICP): effects of source characteristics, noise and spectral bandwidth—'Standard' values for the 50 MHz ICP | Spectrochim. Acta **42B** | 553-579 | 1987 |
| C. W. T. Bulle-Lieuwma & P. C. Zalm *E* | Suppression of surface topography development in ionmilling of semiconductors | Surf. & Interface Anal. **10** | 210-215 | 1987 |
| E. E. Havinga & L. W. van Horssen *E* | Influence of chain length and structural order on the electrical conductivity of poly-*p*-phenylenes heavily doped with potassium | Synth. Met. **17** | 623-628 | 1987 |
| A. G. Tangena *E* | Tribology of thin film systems | Thesis, Eindhoven | 1-129 | 1987 |

*Contents of* Philips Telecommunication and Data Systems Review **45**, No. 1, 1987



Volume 43, No. 9 pages 233-272 Published 23th September 1987

PHILIPS

J. P. van Hemert: Automatic segmentation of speech into diphones,

PhilipsTech.Rev.**43**,No.9,233-242,Sept.1987.

Systems in which synthetic speech is generated often use a library of sound transitions (diphones) as units for forming words in the same way as the letters of the alphabet are used for writing. The libraries are built up by extracting these units from spoken text. This can be done automatically by a combination of two automatic methods. In the first method, boundaries can be placed in words at positions where one steady state changes into another one. In the second method the sounds in a word are compared with reference patterns of particular sounds, and the phonetic identification is assigned to the segments determined by the first method. The second method is also used for correction if too many boundaries or too few are found. The boundaries obtained in this way are not very different from the results obtained by non-automatic methods. With these methods diphone libraries can be built up in a fraction of the time that would be required with a non-automatic method. Evaluation by test subjects of synthetic speech built up from 'automatic' diphone libraries is certainly no worse than that of synthetic speech built up from 'non-automatic' diphone libraries.

D. M. Krol and R. K. Janssen: Research on television glass,

PhilipsTech.Rev.**43**,No.9,253-259,Sept.1987.

The chemical conversions in the melting stage of glass of the composition $15Na_2CO_3$-$10BaCO_3$-$75SiO_2$ have been investigated with the aid of laser-Raman spectrometry. Below 1000 °C a number of different crystalline compounds are formed, whose silicon content increases with increasing temperature. Between 1000 and 1400 °C the melt consists of liquid disilicates or trisilicates, containing dispersed crystalline $\alpha$-quartz. The oxidation/reduction equilibrium of the fining agent antimony in glass whose composition closely corresponds to that of television glass has been studied by potentiometric titration and emission spectrometry. A reaction equation can be written that gives a good description of this behaviour. The possible influence of $NaNO_3$ and cullet on the formation and fining of television glass has also been investigated.

B. Vitt: Black-cobalt coating for solar collectors,

PhilipsTech.Rev.**43**,No.9,244-252,Sept.1987.

In the evacuated receiver tubes of a solar collector an absorber plate with a spectrally selective black-cobalt coating is used for reducing the thermal radiation losses. The influence of the substrate roughness and annealing conditions on the structure and composition of the coatings greatly affects their high-temperature stability and thermo-optical properties. The most suitable coatings for high-temperature application are obtained on smooth substrates after vacuum-annealing at about 450 °C. The optimum electrolytic coating thickness for the required optical selectivity is generally less than 30 C/dm$^2$, depending on the intended temperature range in the collector. The stability of optimized coatings seems to be sufficient for use in solar collectors designed for high-temperature applications (150-250 °C).

L. H. Guildford and B. D. Young: A mobile system for image bulk storage,

PhilipsTech.Rev.**43**,No.9,260-268,Sept.1987.

Often the value of image signals obtained from sources such as TV cameras, night-viewing systems, infrared sensors, ultrasound systems, X-ray equipment and so on, is increased considerably if the images can be recorded faithfully for later analysis or processing. Unfortunately the signal characteristics (e.g. the scanning format) in all these cases can vary greatly. To cope with this variety a versatile system for image bulk storage has been designed around a standard 80-Mbit/s 24-track digital tape recorder. The images can be reformatted either before or after recording by means of an electronic frame store. Images can be replayed on a standard TV monitor or copied on to a computer-compatible magnetic tape for further off-line processing on a mainframe computer. A control computer manages system operation. The application of a sync-block coding scheme permits easy identification and selection of individual images. The image bulk-storage system constitutes a complete transportable laboratory housed in a standard (6.7 m × 2.4 m) shipping container.

# OTHER PHILIPS PUBLICATIONS

**Philips Journal of Research**

A publication in English on the research work carried out in the various Philips laboratories. Published in annual volumes of six issues each of about 100 pages, size 15½ × 23½ cm.

**Philips Telecommunication and Data Systems Review**

A publication in English on systems and equipment for business communications, computer systems and networks, telecommunication services, radio communications and dictation. Published in volumes of four issues, about 40 pages per issue, size 21½ × 29½ cm.

**Electronic Components and Applications**

A publication in English, containing articles dealing with the theory and practice of electronic components and materials. Four issues per year, about 60 pages per issue, size 21 × 29½ cm.

**Medicamundi**

A publication in English on radiology, nuclear medicine and medical electronics. Three issues per volume, about 60 pages per issue, size 21 × 29½ cm.

---

Forthcoming issues of Philips Technical Review will include articles on:

CM12/STEM electron microscope

Metastable phases

Noise in semiconductor lasers

---

Philips Tech. Rev. Vol. 43, No. 9, Sept. 1987

# Contents



PHILIPS TECHNICAL REVIEW
Philips Research Laboratories
P.O. Box 80000
5600 JA Eindhoven
The Netherlands

| | |
|---|---|
| Subscription rate per volume | fl. 80.00 or U.S. $ 35.00 |
| Student's subscription | fl. 32.00 or U.S. $ 14.00 |
| Binder | fl. 10.00 or U.S. $ 4.00 |

Payment only after invoicing, please.

Printed in the Netherlands